DESIGN AND REALIZATION OF A SILICON NANOWIRE PARTICULATE PHOTOCATALYST FOR SOLAR WATER SPLITTING

Taylor Samantha Teitsworth

A dissertation submitted to the faculty at the University of North Carolina at Chapel Hill in partial fulfillment of the requirements for the degree of Doctor of Philosophy in the Department of Chemistry.

Chapel Hill
2021

Approved by:

James F. Cahoon

Scott C. Warren

Joanna M. Atkin

Matthew R. Lockett

Gerald J. Meyer

ABSTRACT

Taylor Samantha Teitsworth: Design and Realization of a Silicon Nanowire Particulate Photocatalyst for Solar Water Splitting
(Under the direction of James F. Cahoon)

Particle suspension reactors (PSRs) offer a cost-effective architecture for solar fuels production via photoelectrochemical water-splitting. However, most previously reported photocatalysts only absorb ultraviolet (UV) or blue light, limiting their possible solar-to-hydrogen energy conversion efficiencies. Silicon absorbs well across the visible and near infrared (IR) spectrum, making it a top choice for photovoltaic modules, but its narrow bandgap does not produce the voltage necessary to split water. Therefore, a multijunction (MJ) particle is required.

Here, we develop the synthesis of high-performance Si nanowire (SiNW) photodiodes and tunnel diodes, allowing for single MJ SiNW solar cells with tunable photovoltages up to at least 10 V under 1-sun illumination. The photovoltage generated by the MJ SiNWs is sufficient to drive the photodeposition of catalytic metals and metal oxides from solutions of metal ions. The axial asymmetry of the potential in the SiNW allows for a spatioselective photodeposition of water-splitting co-catalysts (Pt and CoO_x) and creation of the first Si-based particulate photocatalysts. From prototype PSRs, we find that the spectral dependence of hydrogen generation efficiency is closely related to the photonic characteristics of the sub-wavelength diameter SiNWs. Unlike wider bandgap oxide and chalcogenide materials previously studied for

PSRs, MJ SiNWs bring the advantages of Si to the PSR design, providing a new approach for water-splitting reactors.

Dedicated to my dad who has been my loudest cheerleader during my academic pursuits.

Yes, you may call me “Dr. Breidenbaugh.”

ACKNOWLEDGEMENTS

Thank you to my advisor Professor Jim Cahoon for asking me to do things that I didn't think were possible and never lowering your expectations of me. Even when I doubted myself, you always knew "it should work."

Thank you to the Cahoon lab for creating a such a supportive and energizing place to do science. To my cohort Aaron, Jimmy, and Jon, thank you for going through every step of this crazy process with me. Also, I am especially grateful to Dr. David Hill for his incredible patience with me as I learned how to do everything. You are an excellent mentor and cherished friend.

Thank you to my collaborators in CHANL, the EFRC, Atkin lab, and Kavanagh lab as well as Dr. James McBride for their important contributions to this research.

Thank you to every member of Greenleaf Vineyard Church for praying over me, encouraging me, and doing life with me. I'm not sure I've ever met a group of people who loved science and Jesus so much. I mourn the loss of our community but will forever be grateful for the time we had.

Thank you to my Breidenbaugh and Teitsworth families for supporting me, loving me, pretending you understood what I was talking about, and distracting me from work when necessary.

Most of all, thank you to my dearest Eric. You have endured so much the past 6 years and bore the brunt of my bad days, but you never stopped believing in me. Wherever life takes us after this, I am grateful to have you by my side.

TABLE OF CONTENTS

LIST OF FIGURES

LIST OF TABLES

LIST OF SYMBOLS AND ABBREVIATIONS

A	projected area
AQY	apparent quantum yield
BHF	buffered hydrofluoric acid
CVD	chemical vapor deposition
D	diameter
DI	deionized
D_i	intrinsic segment diameter
DRIE	deep reactive ion etching
$\mathcal{E}$	electric field
E_C	conduction band energy
EDS	energy dispersive x-ray spectroscopy
E_F	Fermi level energy
Eg	bandgap energy
E_V	valance band energy
FF	fill factor
G	generation rate
GC	gas chromotography
HER	hydrogen evolution reaction
I	current
I_o	dark saturation current
IPA	isopropanol
IQE	internal quantum efficiency
I_{SC}	short-circuit current
J	current density
J_{SC}	short circuit current density

k	Boltzmann constant
LED	light emitting diode
L_i	intrinsic segment length
L_n	n-type segment length
L_p	p-type segment length
m^*	effective mass
MJ	multijunction
MMA	methyl methacrylate
N	number of junctions
n	ideality factor
NDR	negative differential resistance
n_e	number of electrons
NW	nanowire
OD	optical density
OER	oxygen evolution reaction
ORR	oxygen reduction reaction
P	pressure
P_{sun}	solar energy flux
PDMS	polydimethylsiloxane
PEC	photoelectrochemical
PMMA	polymethyl methacrylate
PSR	particle suspension reactor
PV	photovoltaic
q	elementary charge of an electron
R_{eff}	effective resistance
r_{H2}	rate of hydrogen production

R_s	series resistance
R_{Sh}	shunt resistance
S	surface recombination velocity
SEM	scanning electron microscopy
s-SNOM	scanning-scattering near field optical microscopy
STEM	scanning transmission electron microscopy
STH	solar-to-hydrogen
T	temperature
TE	transelectric
TEM	transition electron microscopy
TM	transmagnetic
T_{tun}	tunneling probability
UV	ultraviolet
V	voltage
V_{app}	applied voltage
V_{bi}	built-in voltage
vis	visible
VLS	vapor-liquid-solid
V_{OC}	open-circuit voltage
W_D	depletion width
ΔG_{ads}	Gibbs free energy of adsorption
ΔG_{rxn}	Gibbs free energy of reaction
λ	wavelength
Φ	incident photon flux

CHAPTER 1: INTRODUCTION

1.1 Motivation

The rapid pace of technological development over the past two centuries has led to an enormous growth in energy usage[1]. Many tasks that were once completed through human or livestock labor are now performed by machines that require energy input, which has overwhelmingly been provided by carbon-based fossil fuels. While utilization of fossil fuels has undoubtedly allowed for positive development of our society, burning carbon-based fuels has released massive amounts of carbon dioxide, CO_2, a "greenhouse gas" into our atmosphere. Greenhouse gases are small molecules (CO_2, N_2O, CH_3, etc) in our atmosphere that absorb and emit infrared radiation. While a moderate amount of these gases is necessary to insulate our planet from the harsh cold of space, too much can result in detrimental warming of the planet that threatens agriculture, wildlife, and sea-levels. Sustaining and further increasing the quality of life, especially in developing countries, will require even more energy than our current use, and thus it is imperative that we develop more sustainable methods for fuel production that are carbon neutral or carbon negative.

1.2 Photovoltaics and Solar Fuels

The sun irradiates the earth with enough energy to power 10,000 earths at our current global energy usage[2], making it a promising source of clean energy. Capturing, converting, and storing this energy for human use, however, is not a trivial task. The photovoltaic (PV) effect, the generation of electrical current in a material under illumination, was first discovered in metals in

1839 by Becquerel[3], developed further in semiconductor materials[4-6], and eventually became of the basis of our first solar cells. Over the past hundred years of research, the advancement of PV devices (especially silicon devices) has resulted in a high-efficiency, low-cost modules that can be found from residential rooftops to vast fields of solar energy power plants. While PVs are great for capturing and converting light energy into electrical energy, the electricity output from a PV module is related to the intensity and availability of the sun, dropping to zero overnight. Meeting our global energy needs with PVs, which currently account for only 2% of our total global energy production,[7] would require an efficient and likely elaborate method of electrical energy storage and transportation.

Alternatively, sunlight can be converted directly into chemical energy via artificial photosynthesis. Energy stored in gaseous or liquid fuels synthesized with sunlight is much more easily stored, transported, and implemented into our current energy infrastructure. The simplest form of solar fuels production is photoelectrochemical (PEC) water-splitting which produces H_2, an energy dense and carbon-neutral fuel, and O_2, a harmless byproduct. The process occurs via two half reactions: 1) the oxygen evolution reaction (OER) where water is oxidized to form O_2 and protons and 2) the hydrogen evolution reaction (HER).

$$OER: \quad 2H_2O + 4h^+ \rightarrow 4H^+ + O_2$$

$$HER: \quad 4H^+ + 4\,e^- \rightarrow 2H_2$$

$$Net\ Reaction: \quad 2H_2O \rightarrow 2H_2 + O_2$$

The thermodynamic voltage needed to electrochemical split water is 1.23 V, but, due to entropic losses and kinetic overpotentials, the actual required voltage is typically closer to 2 V. PEC water-splitting with a TiO_2 thin film was first reported nearly 50 years ago by Fujishima

and Honda[8]. Unlike PV-modules, these systems are still relatively inefficient and have failed to compete economically with fossil fuels. One major contribution to the cost of a PEC system is the device architecture. PEC designs can be broadly grouped into two categories, shown in Figure 1.1: 1) planar arrays and 2) particle suspension reactors (PSRs)[9,10]. Planar arrays consist of a bulk photoelectrode immersed in an electrolyte solution. PSRs[11], an alternative architecture in which photocatalytic particles are suspended in a plastic bag of electrolyte solution, have received less research attention. An economic and technical feasibility study from 2011 compared these two types of architectures by constructing hypothetical H_2 production plants and accounting for the capital costs, fixed operation and maintenance, decommissioning, and other miscellaneous expenses[10]. Their calculations resulted in a cost per kg of H_2 of \$1.60-3.20 for PSRs and \$4-10 for planar arrays. Even when comparing a PSR system operating at 5% efficiency versus a planar operating at 25%, the cost per kg H_2 was still over 50 cents cheaper in the PSR design. This large discrepancy in cost primarily arises from the inherently simplistic architecture of a PSR that requires fewer components to build and maintain. Therefore, one avenue to achieve economically feasible solar fuels production would be to develop a cheap, stable, and reasonably efficient particulate photocatalyst.

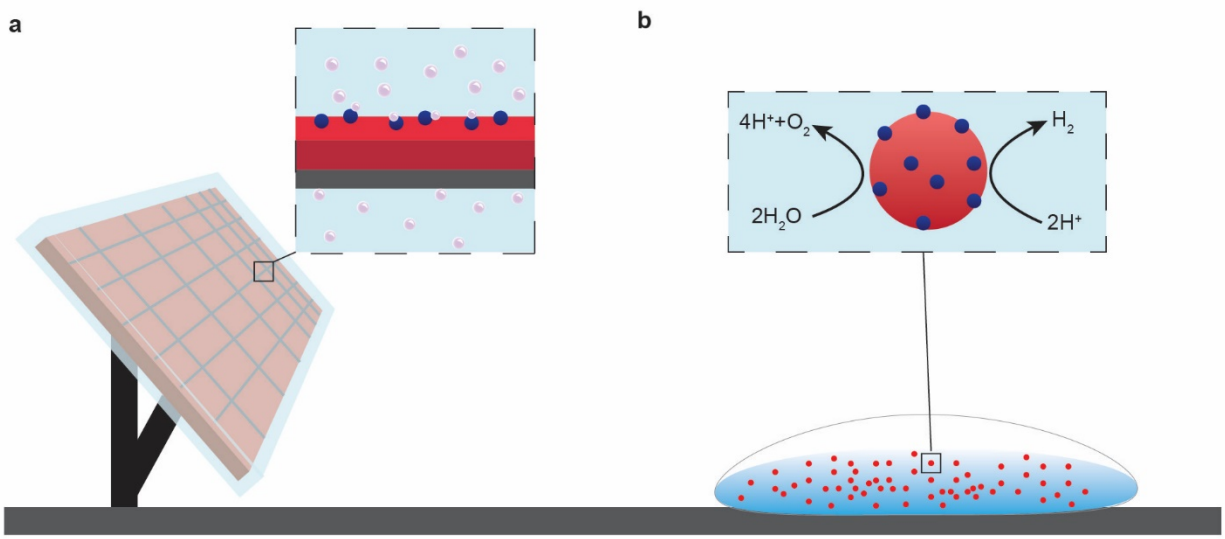

Figure 1.1: Solar water splitting device architectures. **a,** Illustration of a planar PEC solar fuels reactor where aqueous solution is pumped across a planar array. Both products may evolve on the same side of the electrode or they may be generated separated in a tandem or dark-electrode setup (pictured). **b**, Illustration of a PSR PEC architecture, where particulate photocatalysts are suspended in a plastic baggie.

1.3 Photocatalysts for Water-Splitting PSRs

To design effective particulate photocatalysts for solar water-splitting PSRs, we must consider the factors that govern the efficiency of solar fuels production. The equation for determining the solar-to-hydrogen (STH) energy conversion efficiency is

$$\text{STH}\ (\%) = \frac{Chemical\ Energy\ Produced}{Incident\ Solar\ Energy} = \frac{r_{H2} * \Delta Grxn}{P_{sun} * A} x100 \qquad (1.1)$$

where r_{H2} is the rate of hydrogen generated (mol/s), ΔG_{rxn} is the Gibbs free energy of reaction for the water splitting reaction (J/mol), P_{sun} is the incident solar energy flux (J/s*cm^2), and A is the projected area of the reactor (cm^2).

Since the energy produced per split H_2O molecule and the solar energy flux are fixed quantities, the STH efficiency relies on the rate of H_2 production. PEC water splitting occurs in three main steps, illustrated in Figure 1.2: 1) light absorption, 2) charge separation, and 3) redox reaction. Therefore, one can increase the STH of a PEC material by increasing the efficiency of one or more of these processes.

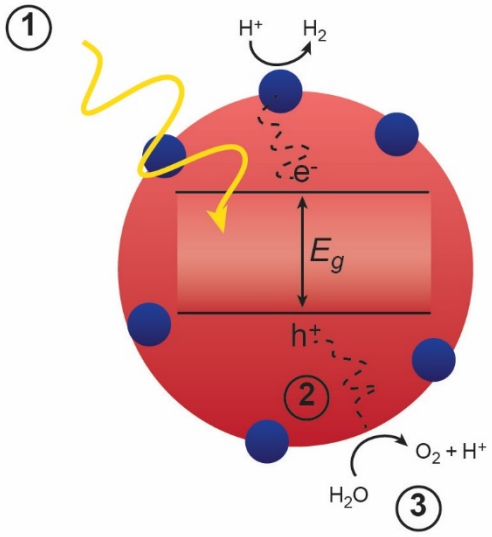

Figure 1.2: Steps of the PEC water splitting process. Illustration of the three fundamental steps of PEC water-splitting, showing 1) light absorption, 2) charge separation/transport and 3) oxidation/reduction reactions.

When a semiconductor absorbs a photon of light, an electron is excited from the valance band to the conduction band, creating an electron-hole pair. For absorption to occur, that photon

must have an energy exceeding the bandgap energy (E_g) of the material. Additionally, for indirect bandgap materials (Si, Ge, etc.), this photon absorption must be coupled with a lattice phonon for electron excitation to occur. Since a majority of solar irradiation comes from visible and infrared light, it would seem advantageous to use a narrow-bandgap material that can absorb a large fraction of the incident photons. However, this is in opposition with the need for a wide bandgap capable of providing sufficient driving voltage. In a recent review of PSR water splitting, a table listing all reported materials had 201 entries for ultraviolet (UV) light-absorbing materials and only 49 entries for visible light-absorbing materials[12]. Most strategies used thus far to increase the efficiency of solar light absorption have been geared towards increasing the light absorption in wide-bandgap materials via valence band engineering[13,14], dye-sensitization[15], and doping[16,17]. Additionally, size effects such as plasmonic resonances in metal nanoparticles[18] and quantum confinement[19] have been used to tune absorption wavelengths into the visible range. The lowest bandgap material demonstrated in a PSR has been $Mn(bpy)V_4O_{11}(bpy)$, a hybrid material with a E_g of 1.6 eV[20].

Once an electron-hole pair is generated, the charge carriers will either remain separated until they reach a surface reaction site or they will recombine, annihilating each other. Recombination most often occurs at mid-bandgap trap states, sometimes introduced by the very same impurities that were incorporated to adjust the light absorption properties. One advantage the particulate catalysts have over bulk electrodes is the short migration distance required to reach the surface sites. Designing specific catalyst geometries that reduce this distance, such as using hollow spheres instead of solid spheres[21], can further increase performance. Introducing material junctions (both homojunctions[22] and heterojunctions[23]) or controlling nanoparticle

faceting[24] can induce built-in electric fields that facilitate charge separation via drift instead of relying on the slower process of thermal diffusion.

Finally, if an electron or hole manages to reach the surface, it needs to transfer to the reactants in solution. The water splitting redox reaction, especially the OER, has a significant kinetic energy barrier that can slow down the reaction rate. Additionally, there are numerous undesirable side reactions that can occur such as the oxygen reduction reaction (ORR). The most common strategy to increase reactivity is to deposit a heterogeneous[25] or homogenous (i.e. molecular)[26] electrocatalyst on the photoabsorber surface that will help adsorb reactants, facilitate charge transfer, and release the desired product. Except in the case where the photoabsorber is capable of catalyzing one of the half reactions, (some metal oxides, for example[27-29]), it is desirable to have two distinct co-catalysts, one for each half-reaction.

In summary, PSRs could be a promising technology for producing solar fuels, but several challenges remain related to the photocatalyst particle design. Most notably, there is a need for visible-light absorbing catalysts, as theoretical calculations show that the highest possible STH efficiency, even in the most ideal case, drops below 10% when the maximum wavelength of absorption is 550 nm (2.25 eV)[30,31]. The solar photon flux is plotted in Figure 1.3 with the absorption onset (based on bandgap) of previously reported visible-light absorbing PSR photocatalysts.

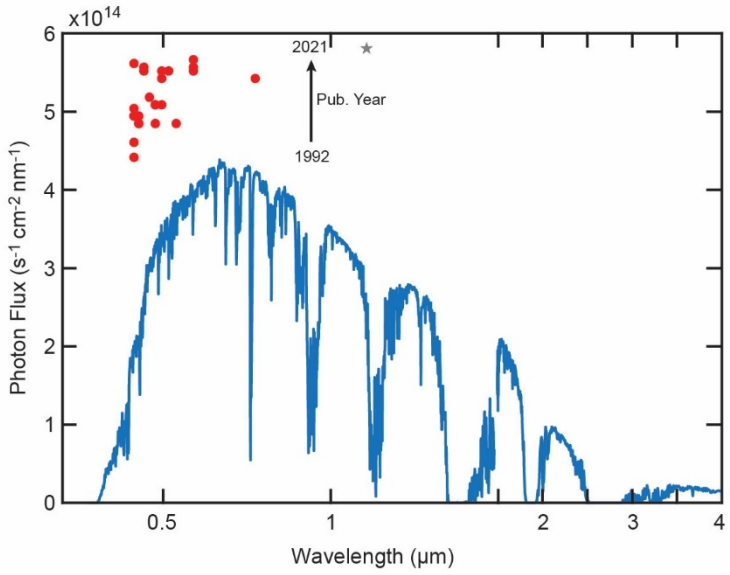

Figure 1.3: Solar photon flux and material bandgaps. The photon flux from AM 1.5 solar irradiation (blue) compared to the absorption onset as determined by the material bandgap of visible light-absorbing particulate catalysts (red circles) reported in Ref. 12 and for silicon (grey star). Data points for absorbers separated by publication year.

1.4 Design considerations for a silicon-based particulate photocatalyst

Silicon (Si) is the second most abundant element on earth and our society is built out of its various forms and compounds: glass, concrete, silicone polymers, computer chips etc[32]. It is no surprise then that Si nanostructures, especially nanowires (NWs) have also gained momentum across a wide range of applications such as biotechnology[33,34], photovoltaics[35-37], electronics[38-40], and plasmonics[41,42]. However, they have been largely precluded from use in artificial photosynthesis due to silicon's narrow bandgap (1.1 eV), which is nearly ideal for optimal solar light absorption but too small to drive PEC water splitting. Triple-junction silicon bulk electrodes have been used to drive unassisted water splitting[43], since the voltage of a multijunction (MJ) can

exceed the material bandgap. The development of a MJ SiNW could bring the benefits of Si (low-cost, earth-abundant, stable, and narrow bandgap) to PSR water splitting. To understand the synthetic requirements for realizing a MJ SiNW, we can break the structure down into its two repeating electronic components: 1) a photodiode and 2) a tunnel/Esaki diode.

1.4.1 Silicon Nanowire Photodiodes

Doping silicon with substitutional impurities changes the electronic behavior of the material. Adding boron or aluminum results in p-type Si, where there is an accumulation of excess holes, while adding phosphorous or arsenic results in n-type Si, where there is an accumulation of excess electrons. Photodiodes are realized by creating p-type/intrinsic/n-type or p-type/n-type (*p-i-n* or *p-n)* doping interfaces. Under equilibrium, electrons and holes diffuse to the p-type and n-type regions respectively until the electric field created by the stationary dopant ions opposes their motion. The resulting structure has two quasi-neutral regions and a depletion region. As seen in Figure 1.4, the conduction and valence bands must bend necessarily to conserve the Fermi level energy.

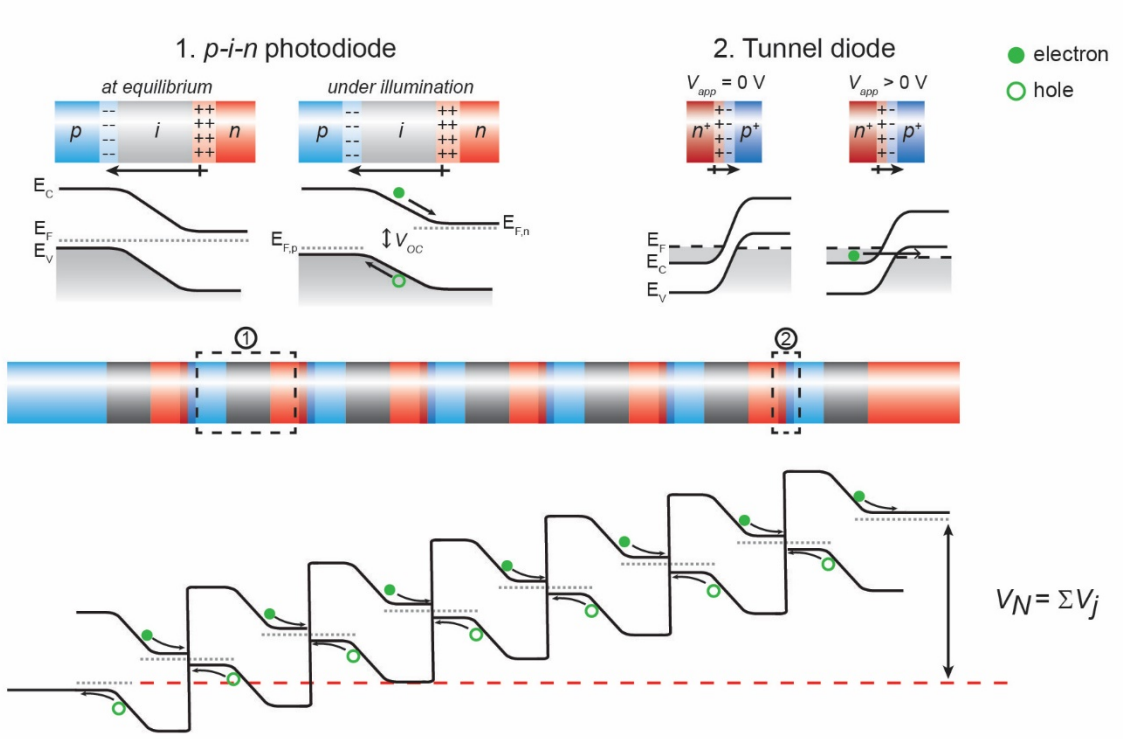

Figure 1.4: MJ PV band structure. Illustrations of the doping pattern and band diagrams for of the conduction band (E_C), Fermi level (E_F), and valance band (E_V) for 1) *p-i-n* diodes (upper left) and 2) tunnel diodes (upper right) are shown. When combined serially, the resulting band structure leads to photovoltage addition, in the absence of shunt or series resistance.

In the dark, the current-voltage (*I-V*) behavior of this device can be described by the ideal diode equation:

$$I = I_0 \left(e^{\frac{qV}{nkT}} + 1 \right) \tag{1.2}$$

where q is elementary charge of an electron, k is the Boltzmann constant, and T is temperature. I_o is the dark saturation current and sometimes also referred to as the "recombination current" as its value increases with the carrier recombination rate[44]. n is the ideality factor used to fit the ideal

diode equation to real diodes and describes the type of dominant recombination mechanism. When recombination in the quasi-neutral region dominates, n =1, and when recombination in the depletion region dominates, n =2 [45]. Previous studies of axial SiNW PVs report values of n of 1.5-2 [35,46,47].

Under illumination, an absorption event creates an electron-hole pair. Carriers generated within the depletion region will be swept by the built-in electric field, with electrons moving towards the n-type region and holes towards the p-type region. Carriers can also be generated in the quasi-neutral regions but their collection relies on diffusion, resulting in a lower charge collection efficiency from these regions. The photocurrent opposes the diode's forward bias current, resulting in the following equation:

$$I = I_0 \left(e^{\frac{qV}{nkT}} + 1 \right) - I_{SC} \tag{1.3}$$

where I_{SC} is the short-circuit photocurrent. In real solar cells, there are numerous sources of parasitic resistance and shunt pathways. Thus, a more realistic equation that includes those effects would be

$$I = I_0 \left(e^{\frac{q(V+IR_S)}{nkT}} - 1 \right) + \frac{V+IR_S}{R_{Sh}} - I_{SC} \tag{1.4}$$

where R_S is the series resistance and R_{Sh} is the shunt resistance[45]. Figure 1.5 shows the *I-V* behavior of a photodiode following these equations. An additional figure of merit for photodiodes is the fill factor (*FF*) which is equal to the max power produced by the diode (P_m) divided by the product of the V_{OC} and I_{SC} and describes the curves squareness.

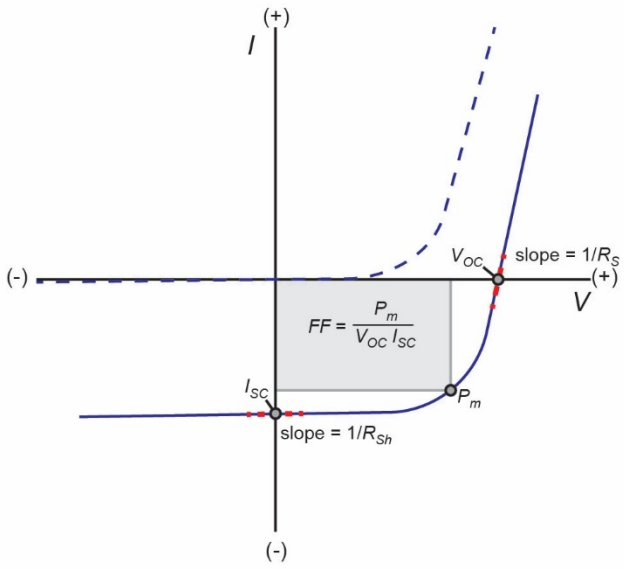

Figure 1.5: *I-V* curve of a photodiode. Illustration of *I-V* behavior described by equations 1.2-1.4 for a photodiode in the dark (dashed blue line) and under illumination (solid blue line) with labeled device metrics.

One of the most studied Si nanoparticle photodiodes is the Si nanowire (NW). SiNWs with *p-n* or *p-i-n* single junctions encoded along their growth axis have been reported in several instances[46,48-50]. Under 1-sun illumination, the single junctions typically generate short-circuit current densities (J_{SC}) of 5-10 mA/cm^2 and open-circuit voltages (V_{OC}) of 0.2-0.4 V. In axial *p-i-n* SiNWs, the surface recombination is the dominant recombination mechanism,[51] thus their performance is limited by surface defects such as dangling bonds, gold deposition, or vapor-solid overcoating. The geometry of the wire, specifically the diameter (D) and intrinsic segment length (L_i), also affects the device metrics and efficiency. For example, by deriving an expression for the surface recombination rate in the cylindrical geometry of a NW, we find that I_o is directly related to the geometry through the following equation[47]:

$$I_0 = q\pi R L_i n_i S \tag{1.5}$$

where R is the nanowire radius, n_i is the intrinsic carrier density, and S is the surface recombination velocity. Although the I_{SC} has been shown to increase with L_i[46,47], this accompanying increase in I_o results in a lower average internal quantum efficiency (IQE), and V_{OC}[47]. The consequences of and interplay between all these parameters must be considered in order to optimize this component of the MJ structure.

1.4.2 Tunnel Diodes

A tunnel or Esaki diode[52] is also a *p-n* junction and has the same electronic band structure; however, the doping levels of both the n and p-type regions are degenerate (i.e. the Fermi levels are in the conduction band and valence band, respectively) and the depletion region width (W_D) is very narrow, on the order of ~10 nm. Although it is energetically unfavorable for an electron to move from the n-type region to the p-type region in this structure, under a very minimal applied voltage the carriers may tunnel from occupied states to unoccupied states on the opposite side of the depletion region via band-to-band tunneling. The tunneling probability (T_{tun}) can be described by the following equation, which assumes a triangular potential energy barrier at the junction[45]:

$$T_{tun} \approx \exp\left(-\frac{4\sqrt{2m^*}E_g^{\frac{3}{2}}}{4q\hbar\mathcal{E}}\right) \tag{1.6}$$

where m^* is the effective mass of the charge carrier, E_g is the material bandgap, $\hbar$ is Plank's constant, and $\mathcal{E}$ is the electric field. Since we cannot change E_g or m^* substantially, the best way to increase the tunneling probability is to increase the $\mathcal{E}$ at the junction by having very high doping levels and a short W_D.

As the applied voltage (*Vapp*) is increased, the tunneling current increases towards a peak current (I_P at $Vapp = V_P$) after which the overlap between the occupied and unoccupied states decreases. This results in a decrease in tunneling current towards a valley current (I_V at $Vapp = V_V$) and a negative differential resistance (NDR) regime, a hallmark of tunneling behavior. The current then increases once the V_{app} is sufficient to induce diffusion. Additionally, if there are trap states in the bandgap, carriers may tunnel through these states instead, resulting in an "excess" current. As shown in Figure 1.6, the total current in a tunnel diode is equal to the sum of the band-to-band tunneling, defect-assisted tunneling, and diffusion currents. In a MJ PV, the tunnel junction allows for energetic equilibration between neighboring *p-i-n* junctions and the addition of photovoltage in series.

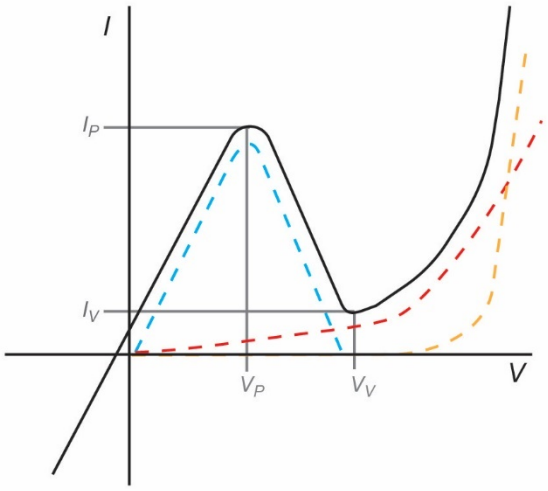

Figure 1.6: *I-V* curve of a tunnel diode. The unique *I-V* behavior of a tunnel diode, where the total current (purple), is equal to the sum of the band-to-band tunneling (cyan), defect-assisted tunneling (red) and diffusion currents (yellow).

For indirect bandgap materials such as Si, the form of the equation for T_{tun} is similar to Eqn 1.6 but must account for the change in effective mass at different points in k-space and for the additional energy needed from a scattering phonon[53]. This results in a comparable *I-V* behavior, but the probability of band-to-band tunneling is much lower and thus the peak current will be lower. However, the valley current, limited by the excess current, tends to be higher in Si than in other direct bandgap materials[54]. Theoretical modelling of the tunneling probabilities in Si has shown that defect-assisted tunneling, which is a direct transition due to the strong localization of the trap state wave function, is much more favorable than band-to-band tunneling except at very high field strengths[55]. Under cryogenic temperatures (liquid He, 4.2K), these defect states are frozen out, the valley current is decreased, and lattice phonons modes can be observed[56].

1.4.3 Multijunction photovoltaic devices

By combining these two optoelectronic components in a *p-i-n* superlattice, we can achieve a MJ PV structure with a certain number of junctions, *N*. As seen in Figure 1.4, under illumination electrons and holes are separated by the photodiodes and then recombine at the tunnel junctions, allowing for voltage addition such that the total photovoltage produced is equal to the total sum of each individual junction. Unlike voltage, the current must be matched in all junctions and one poorly performing photodiode can limit the performance of the entire MJ PV device. Additionally, non-uniform photocurrent generated in adjacent junctions can result in reverse-biasing of poorly performing junctions and cause overheating[57].

To better understand how the performance of our single junctions affects the overall performance of a MJ device, we built a simple model that calculates the *I-V* curve for individual junctions and then adds the voltage together where current is matched, resulting in a MJ *I-V* curve (Code for model can be found in the Appendix). The inset in Figure 1.7a shows the

individual *I-V* curves for five single junctions with metrics similar to those we observe experimentally. The resulting *I-V* curve after voltage addition has a worse FF than the individual diodes (Figure 1.7a, black). By introducing variation to each single junction device metric separately, while keeping all other metrics uniform across the junctions, we can see that the largest effect on device performance is the I_{SC}, highlighting the need for photocurrent matching. Additionally, we can model the effect of tunnel junctions by implementing tunnel junction resistance (R_{TJ}) as a series resistance. An increase in R_{TJ} results in an increased overall R_S and lower *FF* for the device (Figure 1.7b). Also, since the number of tunnel junctions in the device is equal to *N*-1, the overall R_S is expected to increase (and *FF* expected to decrease) as *N* increases (Figure 1.7c).

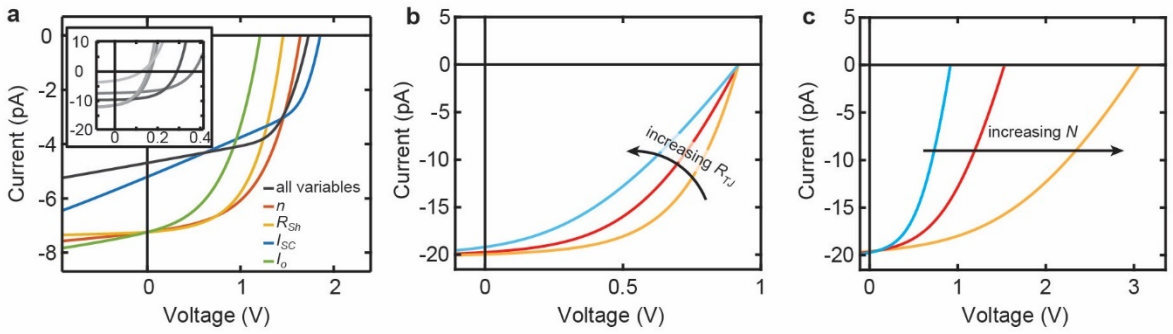

Figure 1.7 MJ PV model. a, *I-V* curves for five single junction PV devices (inset) and a resulting MJ PV device when considering all variations in device metrics (black) and when varying each single diode parameter separately. For cases where only one parameter was varied, all other parameters for each junction were set to the median performing diode in the set. **b,** *I-V* curves from MJ PV devices with a R_{TJ} of 5 GΩ and *N*= 3 (cyan), 5 (red), and 10 (yellow) **c,** *I-V* curves from *N*=3 MJ PV devices with an R_{TJ} of 1 GΩ (yellow), 5 GΩ (red), and 10 GΩ (cyan).

Based on this understanding of MJ PV devices and previous strategies to improve water-splitting efficiency, we propose a SiNW structure with multiple, high-quality, axial *p-i-n* junctions connected by low-resistance tunnel junctions to facilitate spatial charge separation and generate the necessary voltage for water-splitting. Additionally, an HER co-catalyst should be deposited on the SiNW cathode and an OER co-catalyst on the anode to help facilitate reaction of the electrons and holes (Figure 1.8). Herein, we describe the design, realization, and characterization of such a MJ SiNW for PV devices, the deposition of heterogeneous co-catalysts to create a composite particulate photocatalyst, and a prototype PSR capable of unassisted water-splitting.

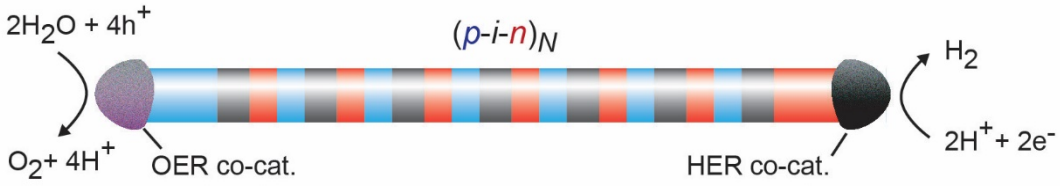

Figure 1.8: Proposed Si particulate photocatalyst. Illustration of a SiNW *p-i-n* superlattice functionalized with heterogenous OER and HER co-catalysts to facilitate charge transfer to molecular reactants.

CHAPTER 2: METHODS

2.1 Nanowire Synthesis

To prepare substrates for SiNW growth, Si/SiO_2 wafers (380 μm thick Si with 600 nm of wet thermal oxide, Nova Wafers) were first cut into 2 cm by 1-3 cm pieces, then briefly sonicated in acetone, rinsed with acetone and isopropanol, dried with N_2, and finally cleaned in UV-Ozone Cleaner (Samco Model UV-1 UV-Ozone Cleaner) for 5 min at 150 ℃ to remove all organic contamination. The substrates were then functionalized with poly-L-lysine (Sigma Aldrich) for 5-10 mins, rinsed with deionized water, and dried with N_2. Au nanoparticles were then deposited by exposing the surface to an Au nanoparticle solution (150 or 200 nm, BBI International) for 5-30 mins, the excess being rinsed with deionized water and dried with N_2. The density of Au nanoparticles, and thus the final nanowire density, increases with time of exposure to the Au solution. The functionalized substrates were cleaned one final time in the UV-Ozone cleaner for 5 min at 150 ℃. Clean tweezers must be used throughout this entire process as even small amounts of contamination can result in failure of the synthesis.

SiNWs were synthesized in a home-built chemical vapor deposition (CVD) reactor with a base pressure of approximately 3×10^{-3} Torr. Substrates were loaded into a quartz tube (22 mm inner diameter, Chemglass Life Sciences) which was heated by a hot-walled tube furnace (Lindberg Blue M, ThermoFisher). Gas flow rates during the synthesis were modulated by mass flow controllers (MKS Instruments). Total pressure of the system was regulated with a 148-J needle valve (MKS Instruments) and monitored with Baratron Capacitance Manometers (MKS

Instruments). All pressure, temperature, and gas flow regulation was done through a custom LabView program. Immediately prior to the synthesis, the quartz tube was heated to 950 ℃ to bake out any adsorbed contaminants. The substrate was then inserted into the quartz tube so that it was centered around the furnace thermocouple and then the tube was depressurized. To ensure no contaminants were present, the process was not started until the pressure of the system was below 4 x 10^{-3} Torr.

Unless otherwise noted, all syntheses were done at 510 °C. Once the furnace reached the growth temperature, the reactor was pressurized to 20 Torr and with the precursor gases and H_2 carrier (Matheson Tri Gas 5N semiconductor grade). Equation 2.1 was used to determine the partial pressure of each precursor in the reactor:

$$P_A = \frac{Q_A}{Q_{tot}} * P_{tot} \tag{2.1}$$

where P_A is partial pressure of species A, Q_A is the volumetric flow rate of A, Q_{tot} is the total flow rate of all gases, and P_{tot} is the total pressure of the system as measured outside of the furnace. The silane (SiH_4, Voltaix) partial pressure was maintained at 200 mTorr, resulting in a growth rate of approximately 300 nm/min at a temperature of 510 °C. Doping level was controlled by modulating the flow of precursor gases diborane (1000 ppm B_2H_6 in H_2, Voltaix) and phosphine (1000 ppm PH_3 in H_2, Voltaix) to achieve an encoded doping level (determined by gas phase ratio) of 7.5 x10^{20} and 5 x 10^{20} cm^{-3} for the p- and n-type segments, respectively. HCl (Matheson TriGas, 5N) gas was flowed at a 2:1 ratio with the SiH_4 to prevent vapor-solid overcoating and gold deposition on the NW sidewalls. Wires were typically nucleated with a short intrinsic section followed by a gradual increase of doping level (over approximately 10 min) into a degenerately doped segment to begin a *p-i-n* or *n-i-p* superlattice. In some cases, the

growth rate was dropped at the tunnel junction (i.e. the *n*-to-*p* or *p*-to-*n* transition) by dropping the partial pressure of the SiH_4 to 20 mTorr while maintaining the same ratios to B_2H_6, PH_3, and HCl. A sample precursor gas flow profile is shown in Figure 2.1.

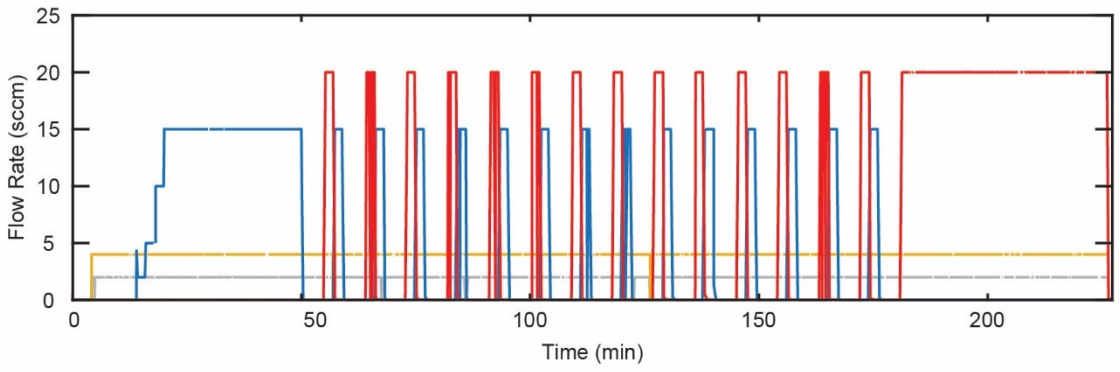

Figure 2.1 Precursor gas flow. Measured flow rate of SiH_4 (gray), HCl (yellow), PH_3 (red), and B_2H_6 (blue) for an N=15 p-i-n SiNW synthesis with a constant growth rate at the tunnel junction.

The growth temperature is perhaps one of the most important conditions for successful MJ SiNW synthesis as it greatly affects the kinetics of dopants incorporation and evaporation. We see a non-intuitive temperature dependence for the boron doping concentration, where the measured active doping level is higher at 510°C than at 650°C. This can be explained by a greater increase in the silicon crystallization rate at higher temperatures that is not matched by the same increase in boron incorporation rate[58]. Since the doping level of our SiNW is dictated by the kinetics instead of thermodynamics, we are able to achieve non-equilibrium doping levels above the solid solubility of B in Si[59]. Additionally, the temperature influences the dopant reservoir effect, where dopant atoms remain in the Au catalyst after the precursor flow is turned off and continue to incorporate into the wire[60,61]. The n-type-to-intrinsic dopant transition is

much broader when grown at 650°C compared to 510°C which is likely due to desorption of hydrogen from the Au catalyst surface at higher temperatures, inhibiting the evaporation of P atoms as PH_3 [58].

2.2 SiNW Etching

SiNWs were transferred to a small clean piece of Si wafer coated with 100 nm wet thermal oxide and 200 nm low pressure CVD Si_3N_4. The substrate was then immersed in buffered hydrofluoric acid (BHF improved, Transene) for 10 s, two water rinse solutions for 10 s each, isopropanol for 30s, a 20 wt% potassium hydroxide (KOH) solution for a specified amount of time, a 2% acetic acid solution 15 s, a water rinse for 10 s, a final isopropanol rinse for 10 s, and then dried with N_2. When necessary, a gold etch was used to remove surface gold from the wires prior to the KOH etch. This process involves first removing the thin SiO_2 layer on the gold surface (10 s BHF, 10 s water, 10 s, water, dry in N_2) and then immersing in Au-etching solution of 4:1:40 (w/w/w) $KI:I_2:H_2O$ for 30-60 s.

2.3 Co-catalyst Photodepositions

After NW growth, a thin layer of SiO_2 is formed on the surface of the Au catalyst. Therefore, a 10 s BHF etch prior to photodeposition is required to achieve uniform deposition and failure to remove the oxide will result in a failed or uneven deposition (Figure 2.2a-c). The substrate was then rinsed in water and transferred immediately to a small polymethyldisulfonate (PDMS) well without drying in order to prevent NW collapse. Precursor solution was added to the well, covered with a glass slide to prevent evaporation, and illuminated under a 1 kW Xe lamp solar simulator (Newport model 91191) with an AM1.5G filter for a specified length of time (typically 10 mins). Unless otherwise noted, photodepositions were performed under ~5 sun

illumination. A list of precursor solutions used are listed in Table 2.1. Anneals and other post-deposition treatments of these wires must not exceed the Au-Si eutectic temperature of 363℃ or the Au tip will melt and destroy the co-catalyst attachment (Figure 2.2d).

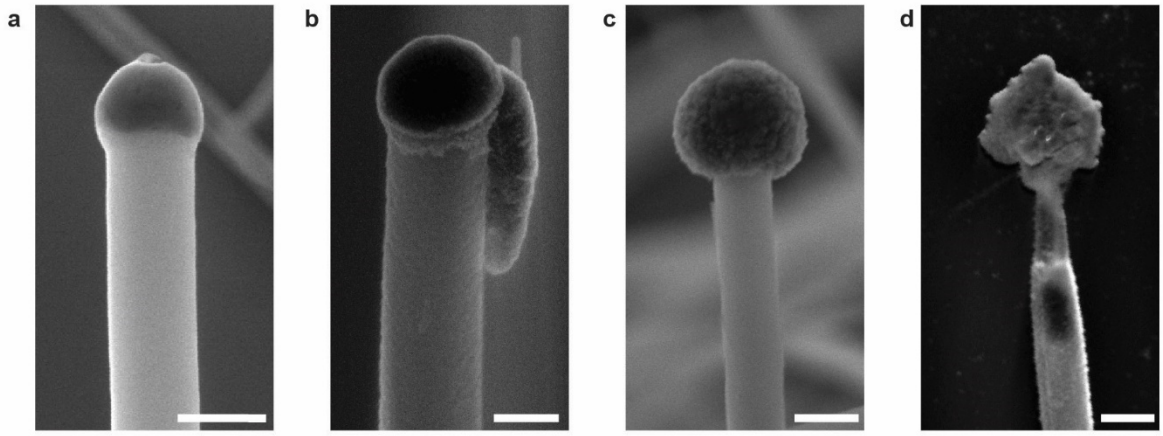

Figure 2.2 Pt photodepositions on Au tip of N=15 MJ SiNWs a, Pt deposition with no prior surface treatments or etching. Scale bar, 200 nm. **b,** Pt photodeposition on wires etched in dilute BHF solution. Scale bar, 100 nm. **c,** Pt photodeposition on wires etched in BHF, Scale bar, 200 nm. **d,** Pt deposition annealed in 5% H_2 at 600℃. Scale bar, 200 nm.

Table 2.1: List of photodeposition precursors

Deposited Material	Precursor Solution (aq)
Pt	5 mM H_2PtCl_6
Cu	5 mM Cu(I)Cl
Fe	5 mM Fe(III)NO_3
Rh	10 mM Rh(III)Cl_3 xH_2O
MnO_x	5 mM $Mn(NO_3)_2$ x4H_2O
CoO_x	5 mM $Co(NO_3)_3$
FeO_x	6 mM Fe(II)Cl_2

Sequential co-depositions were done by first functionalizing the Au tip while the SiNWs were still on the growth substrate. The substrate was then rinsed in water, re-etched in BHF, and sonicated into a vial containing the next photodeposition solution. The bare substrate chip was removed from solution and a stir bar was placed in the vial. The vial was placed on a stir plate set to a low speed under the solar simulator lamp. Deposition rates are typically higher on the suspended wires, so deposition times were shorter (3 to 5 minutes). The deposition solution was then centrifuged at 6000 rpm for 20 minutes (Fisher Scientific accuSping 1R), resulting in a SiNW "powder" at the bottom of the tube. The supernatant was removed with a pipette and the wires were resuspended in 5-10 mL of water. This centrifugation process was repeated for a total of 2-3 times in order to remove as much residual precursors as possible.

2.4 Imaging

Optical bright-field and dark-field microscopy was performed on a Zeiss Axio Imager A.2m upright microscope. Near-field microscopy experiments, performed by the Atkin group, used a home-built infrared s-SNOM system based on a modified commercial AFM (Bruker Innova) as described previously[62]. A vertically-polarized CO_2 laser (Access Lasers) at 10.6 μm wavelength was used as an excitation source. The near-field signal was demodulated at the third harmonic of the tapping frequency and used to construct an optical image simultaneously with the AFM topography. s-SNOM experiments were carried out using a homodyne interferometric scheme, utilizing a two-step procedure to calculate the near-field phase and amplitude[63]. To allow for comparison of the near-field signal across samples, SiNWs were deposited onto Au-coated Si_3N_4 substrates and were normalized to the high-intensity, spectrally flat signal from the Au surface. Near-field spatial resolution was determined from near-field approach curves to be ~10 nm. Several scans (2 × 2 μm, 512 × 512 pixels) were taken along the length of the wire to

observe the doping profile. These images were then stitched together to provide a map of the multiple *n*-*i*-*p* junctions along the SiNW length. Doping assignments were determined by comparing the near-field phase and amplitude to the encoded doping profile. The *n*-type sections were shown to have the highest near-field amplitude, with *p*-type sections having a lower amplitude but higher phase, and intrinsic Si having the lowest amplitude and phase. This agrees with previously established s-SNOM carrier sensitivity levels[62].

All scanning electron microscope (SEM) images were acquired on a FEI Helios Nanolab at 5 kV accelerating voltage and 86 pA. For transmission electron microscopy (TEM), scanning transmission electron microscopy (STEM) imaging, and energy dispersive spectroscopy (EDS), NWs were transferred to lacey-carbon TEM grids (Ted-Pella no. 01895) by dipping the grid into a dilute suspension of functionalized wires. TEM and STEM-EDS was performed on a Tecnai Osiris HRTEM/STEM operating at 200 kV equipped with a SuperX™ quad EDS detection system. STEM-EDS maps were collected using Bruker Esprit software version 1.9 with a sub-nm probe having ~ 0.8 nA of beam current. The drift-corrected STEM-EDS maps were typically collected over a 5 min period. Some TEM and STEM-EDS images were collected under similar conditions on a Thermo Scientific Talos F200X equipped with Velox imaging software.

2.5 Device Fabrication

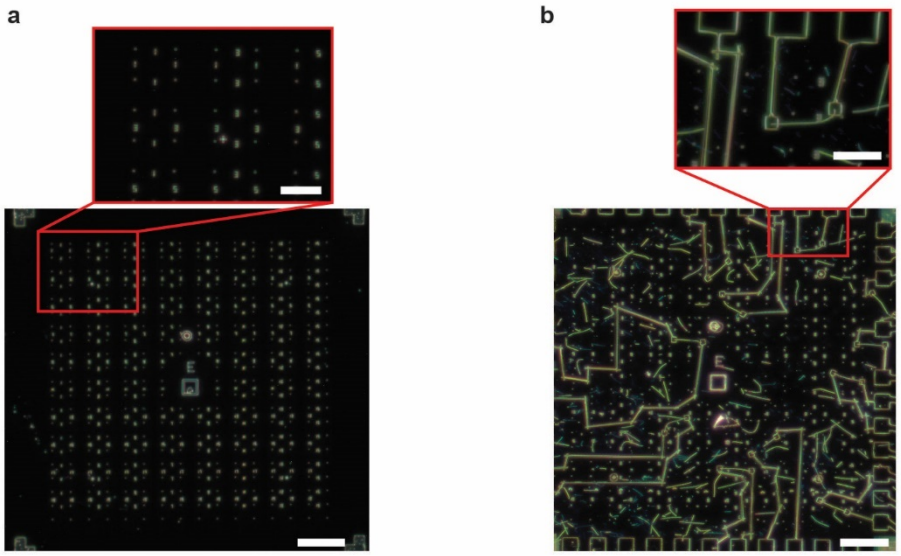

Figure 2.3: Single NW Device Fabrication. a, Dark field microscopy image of a device marker pattern with a zoomed-in image of the number array used to locate wires of interest. **b,** Dark field microscopy image of a PV device chip with multiple SiNW PV devices and a zoomed-in image of a single NW device with a metal contact on each side. Scale bars in both panels are 100 µm (lower) and 40 µm (upper).

2.5.1 Marker Patterns

All devices were constructed on pre-fabricated marker patterns, seen in Figure 2.3a, fabricated on Si wafers coated with 100 nm wet thermal SiO_2 and 200 nm plasma-enhanced CVD Si_3N_4 (Nova Electronic Materials). A photoresist stack (MMA EL 9 and PMMA A7, Microchem) was spun onto the wafers and a number grid was patterned using electron-beam lithography (Nanometer Pattern Generation System) on a FEI Helios 600 SEM with an accelerating voltage of 30 kV, beam and dosage of 350 µC/cm^2. The patterns were developed for

1 minute in methyl isobutyl ketone (MIBK, 1:3 solution in IPA, MicroChem), rinsed in IPA, and dried with N_2. The patterned area was etched away using a deep reactive ion etcher (DRIE, Alcatel AMS 100). The top SiO_2 and Si_3N_4 layers were etched for 3 minutes with 20 sccm of C_4F_8 and 150 sccm of Ar at a position of 25%, source power of 1000W, and substrate holder power of 75W. The underlying Si layer was then etched for 45 s with 100 sccm of SF_6 and 100 sccm of Ar at a position of 25%, source power of 500 W, and substrate power of 50 W. This results in a total etch depth of approximately 1 μm, which can easily be seen under the SEM in the subsequent lithography steps.

2.5.1 Tunnel Junction Devices

SiNWs were mechanically transferred from the growth substrate by gently touching the surface to a marker pattern. A photo-resist stack (MMA EL9 and PMMA A2, Microchem) was spun on top of the NWs and contacts to single NWs were patterned via electron beam lithography (Nanometer Pattern Generation System). The native oxide was etched from the patterned area using buffered hydrofluoric acid (BHF Improved, Transene) and metal electrodes (3 nm Ti, 300 nm Pd) were deposited with electron beam evaporation (KJ Lesker PVD 75). Each NW was contacted by four electrodes with two contacts on each side of the junction to ensure that the contacts were ohmic.

2.5.2 Single Nanowire PV Devices

For PV devices, NWs were mechanically transferred onto pre-fabricated marker patterns. Unless otherwise noted, the device chips with SiNWs were annealed under 760 Torr forming gas (5% H_2 in N_2, Airgas) in a rapid thermal annealing system (ULVAC MILA-5000) by quickly heating to 600 ℃ and ramping down to 300 ℃ over 2 hours. An electron-beam photoresist stack

(MMA EL 9 and PMMA A2, Microchem) was spun onto the wires and contacts were patterned to the wires via electron-beam lithography (Nanometer Pattern Generation System) using an FEI Helios 600 Nanolab dual-beam system. The native oxide on the contact area was etched using BHF and metal contacts (3 nm Ti, 300 nm Pd) were deposited immediately using an electron-beam evaporator (Kurt Lesker PVD 75) at a base pressure of ~$2x10^{-8}$ Torr. Excess metal and residual MMA was removed by soaking in acetone for 15-30 mins, rinsing in acetone, and then drying N_2. An image of a finished device is shown in Figure 2.3b.

2.5.3 Single Nanowire Electrochemical Cells

MJ SiNWs previously co-functionalized with Pt and CoO_x were dropcast from a suspension in water onto a prefabricated marker pattern. Bright field optical microscopy was used to identify which end of the wire was the working electrode and then electron-beam lithography and electron-beam evaporation were used to deposit Ti/Pd contacts on one end of the wires (either *n*- or *p*-type) using the same procedure as the PV devices. Directly after metal evaporation, SiO_2 (75-100 nm) was deposited by electron beam evaporation (Thermionics VE-100) on the metal contacts. An SU-8 polymer (SU-8 2000.5, Microchem) was also patterned by electron-beam lithography over the metal contacts and the majority of the SiNW, leaving the NW tip exposed to solution. In preliminary device tests, only the SU-8 layer was used but we found this was not sufficient to prevent a large background current. To create the liquid cell, a square PDMS (Dow SYLGARD 184) well with a thickness of 3 mm was cut using a clay punch (NS Creative Elements) to have outer dimensions of 6 x 6 mm and inner of 3 x 3 mm and was secured onto the chip by painting a thin layer of PDMS two-part solution onto the bottom of the well and then curing it to the chip surface by heating on a hot plate at 100°C for 30-45 mins.

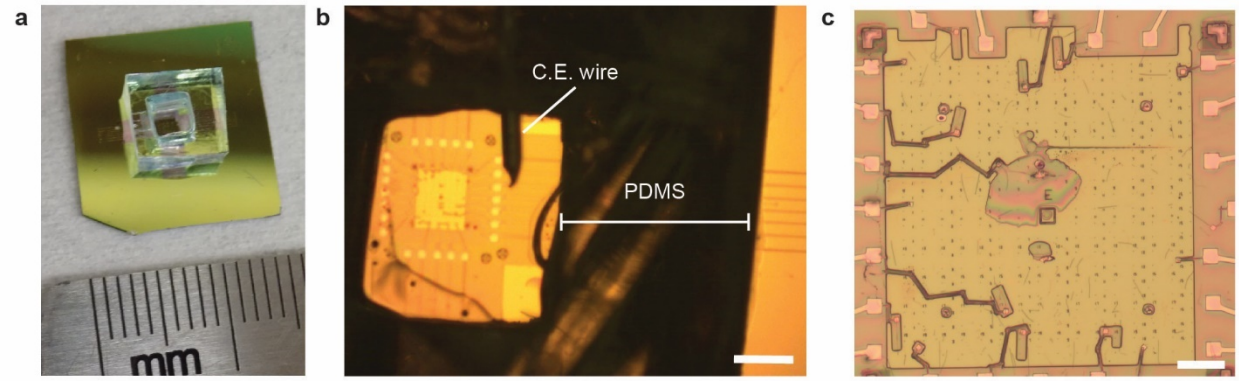

Figure 2.4 Single SiNW electrochemistry cell. a, Photo of a complete single NW electrochemistry cell with ruler to show scale. **b,** Microscope image of cell with counter electrode inserted through the sidewall. Scale bar, 1 mm. **c,** Microscope image of wires in the inner section of the device pattern after SU-8 patterning. Scale bar, 100 µm.

2.6 Device Measurements

2.6.1 Tunnel Junction Devices

Electrical measurements were taken with a Keithley 2636A SourceMeter connected to a cryogenic probe station (Lakeshore PS100). For low temperature measurements, the devices were put under vacuum and cooled with liquid nitrogen. Prior to measuring across the junction, measurements were taken on the *p*-type and *n*-type ends to ensure the contacts were ohmic. Junction resistance was estimated by fitting the low bias region (-0.1 to +0.1 V) of the current-voltage *(I-V)* curve to a linear equation to determine the resistance (*R*), equal to the inverse of the slope. An effective resistance of the junction was then calculated by multiplying *R* by the cross-sectional area of the wire, as determined by SEM.

2.6.2 Single Nanowire PV Devices

PV measurements were taken with a Keithley 2636A SourceMeter connected to a home-built probe station consisting of Signatone micromanipulators (S725) and tungsten probe tips (SE-TL). A 1 kW Xe lamp solar simulator (Newport model 91191) with an AM1.5G filter was calibrated to 1-sun (100 mW/cm^2) with a reference Si photocell (Newport model 91150 V) and was used to illuminate the SiNW devices. For measurements under increased illumination, the light from the lamp was concentrated over the device area using a lens. Device characteristics under illumination were calculated by a linear fit to the x and y intercepts of the light *I*-*V* curve. A linear fit of the semi-log plot of the dark curves was used to get an estimate of n and I_o, but parasitic resistances made these values unreliable especially as N increases. Therefore, these values were used as initial guesses to fit the dark *I*-*V* curves to a modified ideal diode equation[45,64] that includes a series resistances. For our fitting equation we included R_S but assumed an R_{Sh} of infinity.

2.6.3 Single Nanowire Photoelectrochemistry

Two-electrode photocurrent measurements were taken with the functionalized SiNW as the working electrode and a macroscopic wire, inserted through the side of the PDMS well, as the counter electrode. For photocathode measurements (i.e. the *n*-type/Pt-functionalized tip exposed to solution), an iridium wire was first placed in a UV-Ozone cleaner for 10 minutes to clean carbon contaminants and oxidize the surface and was then used as the counter electrode. Using the home-built probe station, the MJ SiNW devices were connected to the counter electrode through the Keithley SourceMeter. Photocurrent at zero applied bias was measured under illumination from an LED light source (Lumencor Spectra X Light Engine) at 445 ± 20 nm (44.6 mW/cm^2), 549 ± 10 nm (55.9 mW/cm^2), and 650 ± 13 nm (28.8 mW/cm^2). Colored LEDs

were used instead of the 1-sun simulator due to a large background current present under UV and IR illumination wavelengths. The IR seemed to induce especially large currents, likely due to absorption by the metal contacts. Similar measurements were done for the photoanode (p-type Si/CoOx functionalized base) but with a Pt wire counter electrode that was cleaned in BHF to remove any surface contaminants and oxide layer.

2.7 Particle Suspension Reactors

Co-functionalized MJ SiNWs were suspended in a pH 3 H_2SO_4 (aq) solution in a home-built quartz reactor fitted with a stainless-steel cap and Swagelok outlet/inlet valves. The solution was stirred and purged with argon gas for approximately one hour. The reactor was then closed and illuminated with an LED source (Lumencor Spectra X Light Engine) at wavelengths of 445 ± 20, 485 ± 20, 549 ± 10, and 650 ± 13 nm. The fiber optic cable directing the illumination was mounted such that the diameter of the beam was the same width as the reactor sidewall (1.5 cm) and illuminating almost the entire area of the suspension. Headspace samples (~0.5 mL) were extracted from the outlet valve using a Luer-lok syringe and injected into a gas chromatograph (GC, Varian 450). Concentration of H_2 gas was determined using a calibrated pulsed discharge helium ionization detector. Moles of H_2 were calculated using the volume of the reactor headspace plus the syringe, assuming ideal gas behavior. The reactor was purged for 20-30 minutes with argon in between trials. NW density in the PSRs was estimated by drop casting a known volume of the suspension and using SEM to count full-length NWs over a measured projected area for extrapolation of the total number of SiNWs in the volume.

2.8 UV-Vis Spectroscopy of NW suspensions

Extinction and absorbance spectra of the suspensions were measured on a UV-Vis Spectrophotometer (Cary-5000, Agilent) using a cuvette with 1 cm path length. For the

absorbance measurements, the diffuse reflectance accessory (e-DRA) equipped with an integrating sphere was attached to the instrument and the cuvette was placed in the center position to capture the transflectance. Optical density (OD) of the PSRs in the reactor was determined by multiplying the extinction by the reactor thickness.

2.8 Optical Simulations and Calculations

Absorption, scattering, and extinction spectra for single SiNWs were calculated with finite-element modelling in COMSOL Multiphysics version 5.4. The simulation geometry, pictured in Figure 2.2, included a 32 μm long Si cylinder divided axially into ten 3.2 um *p-i-n* segments to represent an $N = 10$ MJ SiNW. The cylinder was surrounded by 200 nm of air on all sides with refractive index of one and a perfectly matched layer (pml) on all sides. The NW was illuminated with a plane wave where the wavevector, k, was determined by

$$k = k_a[\sin -\theta\ \hat{\boldsymbol{y}} - \cos\theta\ \hat{\boldsymbol{z}}] \tag{2.2}$$

where k_a is the free space wavenumber and θ is the angle of incidence with respect to normal. The background electric field (E_b) was calculated by

$$E_b = [E_0 \exp(-ik)\sin\beta]\,\hat{\boldsymbol{x}} + [E_0 \exp(-ik)\cos\beta\cos\theta]\,\hat{\boldsymbol{y}} + [E_0 \exp(-ik)\cos\beta\sin\theta]\hat{\boldsymbol{z}} \tag{2.3}$$

where E_0 is the field strength (10000 V/m), and β is the polarization angle. β is set to 0° for transmagnetic (TM) and 90° for transelectric (TE) polarized illumination. The illumination intensity, I_0 (1.32×10^5 W/m^2), was uniform across all illumination wavelengths.

For each illumination angle, the absorbed power in each segment was calculated for both the TE and TM polarization from 400-1000 nm at 5 nm intervals and the two spectra were averaged to determine the unpolarized result. The average spectrum was then divided by I_0 and

multiplied by the solar irradiance spectrum to correct for the absorption under 1-sun illumination. The absorbed power was converted to absorbed photons and integrated to determine the photocurrent generation, assuming an internal quantum efficiency (IQE of unity). This model was run for illumination angles in 10° increments (0, 10, 20, 30, 40, 50, 60, 70, 80, and 90°) and interpolated to 1° increments. A weighted average of the photocurrent was calculated assuming a three-dimensional isotropic distribution of the SiNW orientation in solution.

Scattering was calculated by integrating the Poynting vectors over the NW surface for TE and TM polarizations and taking an average of the two spectra. The extinction spectra were calculated by summing the scattering and absorption spectra.

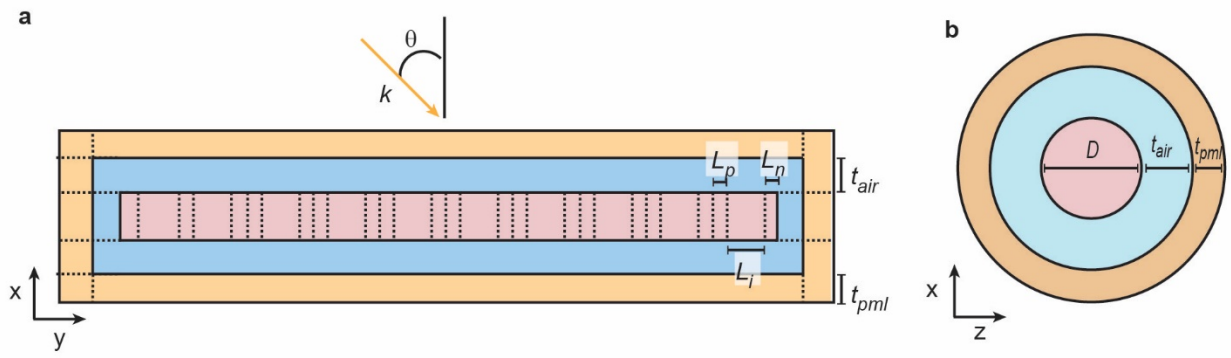

Figure 2.5: COMSOL optical simulation geometry. a, the side-on view and **b,** coaxial view of the simulation geometry of the COMSOL model for light absorption and scattering calculations. Solid lines denote material interfaces while dashed lines signify separate domains within the same material for the purpose of meshing and calculations. L_i, L_p, and L_n are the lengths of the intrinsic, p-type, and n-type segments. t_{air} and t_{pml} are the thicknesses of the air and pml layers. D is the NW diameter.

Photocurrent for a bulk, planar $N = 10$ Si PV device, with each junction of a thickness equivalent to the length of junctions in the SiNW, was calculated analytically by solving for the carrier generation rate (G) at distance x from the surface from known absorption coefficients[65] using the following equation

$$G(\lambda) = \alpha \Phi e^{-\alpha x} \tag{2.4}$$

where α is the wavelength-dependent absorption coefficient of Si and Φ is the incident photon flux. The absorbed photons were then integrated over each 3.2 μm segment assuming zero reflection from the surface.

CHAPTER 3: SILICON NANOWIRE MULTIJUNCTION PHOTOVOLTAIC DEVICES

3.1 Introduction

The ability to synthesize a MJ SiNW photovoltaic device would continue to open up the application space of SiNWs, including PEC water splitting. SiNWs can be synthesized by several methods such as top-down etching of micropatterned silicon wafers[66] or bottom-up growth on metal catalysts in liquid solutions[67] or vapor atmospheres[68]. The gold-catalyzed vapor-liquid-solid (VLS) mechanism, first demonstrated at Bell Labs in 1964[69], takes advantage of the gold-silicon eutectic phase diagram and allows for single crystal silicon NWs to be grown layer-by-layer with very precise control over growth parameters (growth rate, impurity concentration, etc.), making it the most promising method to achieve the required dopant modulation for a MJ SiNW PV. Additionally, the diffusion coefficients of B and P in Si are negligibly small at typical VLS growth temperatures[59,70], preventing dopant diffusion during long synthesis times.

Despite a report more than 10 years ago of a SiNW with two *p*-*i*-*n* junctions, yielding a V_{OC} of ~0.4 V[46], the challenging synthetic requirements for VLS growth of a *p*-*i*-*n* superlattice has barred further experimental development. Additionally, the low solid solubility of boron in Si[59] and the reservoir effect[71] have impeded the realization of a SiNW tunnel diode and, until very recently, the only reported success was an n-type wire grown on a degenerately doped p-

type wafer[72]. Our investigation of the kinetics of VLS-growth under various conditions has allowed for precise synthetic control and realization of complex doping structures. Recently, we have reported growth conditions that yield SiNWs with degenerate doping levels, sharp dopant transitions, no evident vapor-solid radial overcoating, and minimal gold (Au) loss[58,61,73], providing the prerequisite synthetic requirements to yield SiNW *p-i-n* superlattices and high-doped, abrupt tunnel junctions[74] for usage as MJ PVs. Here we describe the synthesis and characterization of the first VLS-grown SiNW tunnel junctions and first MJ PVs with greater than two junctions.

3.2 Results and Discussion

3.2.1 SiNW Tunnel Junctions

SiNWs with a diameter of ~200 nm were grown via the VLS growth mechanism in a home-built CVD system that allowed for rapid precursor flow modulation. The wires were grown in both the n-to-p and p-to-n polarities and the junction was formed by abruptly switching the dopant precursor from phosphine (PH_3) to diborane (B_2H_6) or vice versa. Encoded doping levels (determined by ratio of Si to B/P gas phase precursor mixture) were $5x10^{20}$ and $7.5x10^{20}$ cm^{-3} for the P and B doping respectively, but previous resistivity measurements show that the active doping is closer to 4-5 $x10^{19}$ cm^{-3} for both dopants[58,61]. Since previous studies on VLS-growth SiNWs superlattices show that lower growth rates can facilitate sharper dopant transitions[61], we also synthesized junctions where the growth rate was dropped by an order of magnitude by dropping the SiH_4 partial pressure while retaining the same carrier gas flow rate (Figure 3.1). Here, we will refer to the SiNWs without a growth rate drop as “Growth 1” and those with a growth rate drop as “Growth 2”.

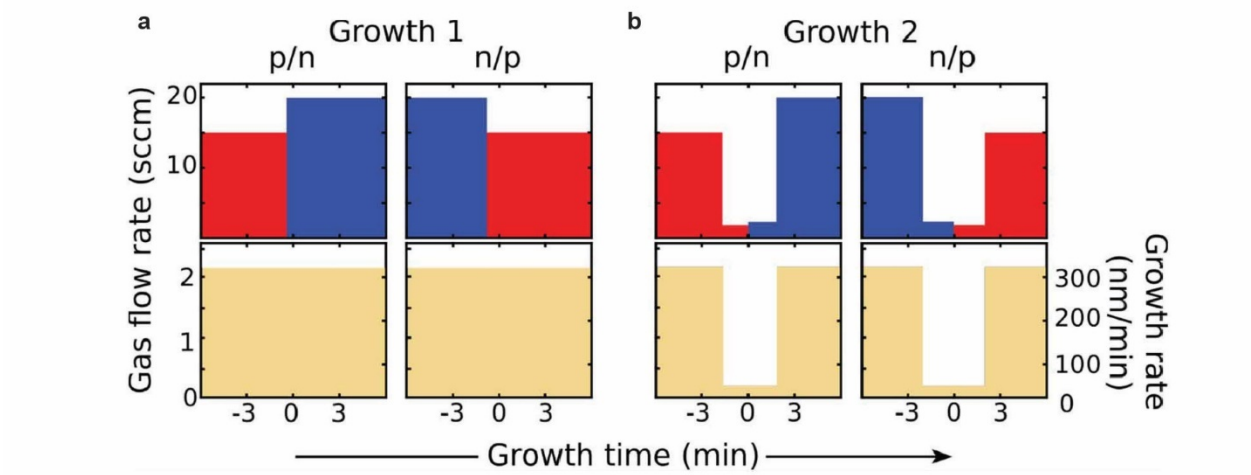

Figure 3.1 Flow profile of precursor gases in SiNW tunnel diodes Flow rates of B_2H_6 (red), PH_3 (blue), and SiH_4 (tan) for abrupt p-n and n-p junctions where **a,** the NW growth rate is a constant 300 nm/min and **b,** the growth rate is dropped to 30 nm/min at the junction.

Off-axis electron holography (EH) is a transmission electron microscopy (TEM) method that measures the phase change of the electron beam as it passes through a sample via superposition of an interference and reference wave image[75] and can be used to determine the electrostatic potential change in axial NW *p-n* junctions[76]. EH measurements, taken by collaborators in the Kavanagh group at Simon Fraser University, were used to determine the built-in potential (V_{bi}) and W_D for each our SiNW tunnel junction growth conditions. TEM images of Growth 1 junctions show a relatively smooth surface with no morphological changes at the junction (Figure 3.2 c-d). Linear profiles of the EH phase maps (Figure 3.2 e-f) were taken to extract a V_{bi} of 1.17 ± 0.02 and 0.86 ± 0.01 V and a W_D of 19 ± 2 nm and 12 ± 1 nm for the *p-n* and *n-p* growth polarities respectively (Figure 3.2 g-h), which agrees well with the bandgap of Si. For Growth 2, we observe no morphological changes for the *p-n* growth polarity but see a small bump in the *n-p* growth polarity (Figure 3.3 c-d). Linear profiles of the potential drop yield

a V_{bi} of 1.02 ± 0.02 and 0.8 ± 0.3 V and a W_D of 10 ± 1 nm and 77 ± 20 nm for the *p-n* and *n-p* growth polarities respectively (Figure 3.3 e-h).

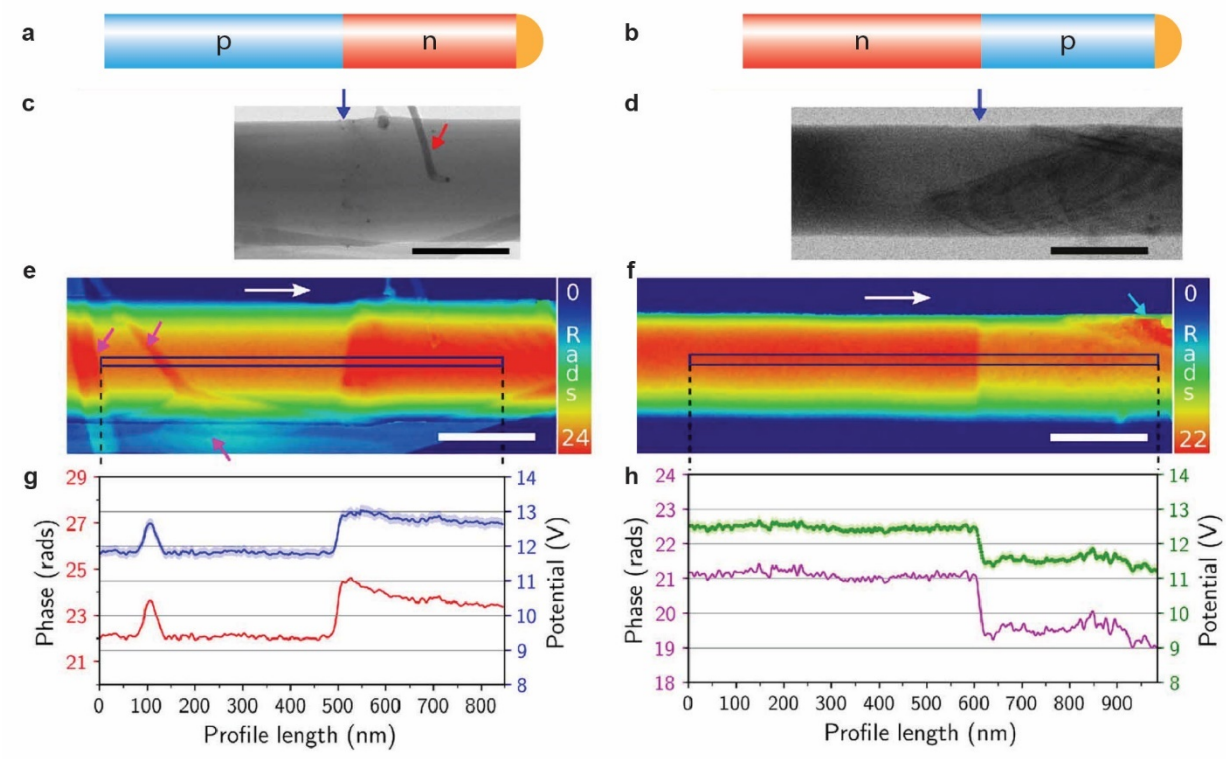

Figure 3.2: EH of Growth 1 tunnel diodes. a, *p-n* and **b**, *n-p* growth sequence schematics (not to scale). **c-d** Bright-field TEM images of the region nearby the p-n junction. Blue arrows indicated the location of the *p-n*/*n-p* junction. Scale bars are equal to 200 nm. **e-f,** Pseudo-colored phase images where the white arrows indicate growth direction while fuchsia and cyan arrows mark presence of TEM grid and a phase unwrapping artifact, respectively. Color bar is in units of radians and scale bars are equal to 200 nm. **g-h** corresponding 1-dimensional phase and calculated potential profiles taken along the center axis of the NWs as shown by the boxed regions in panels e and f. The blue and green error bands in g and h correspond to the error added by the native oxide on the electron beam direction.

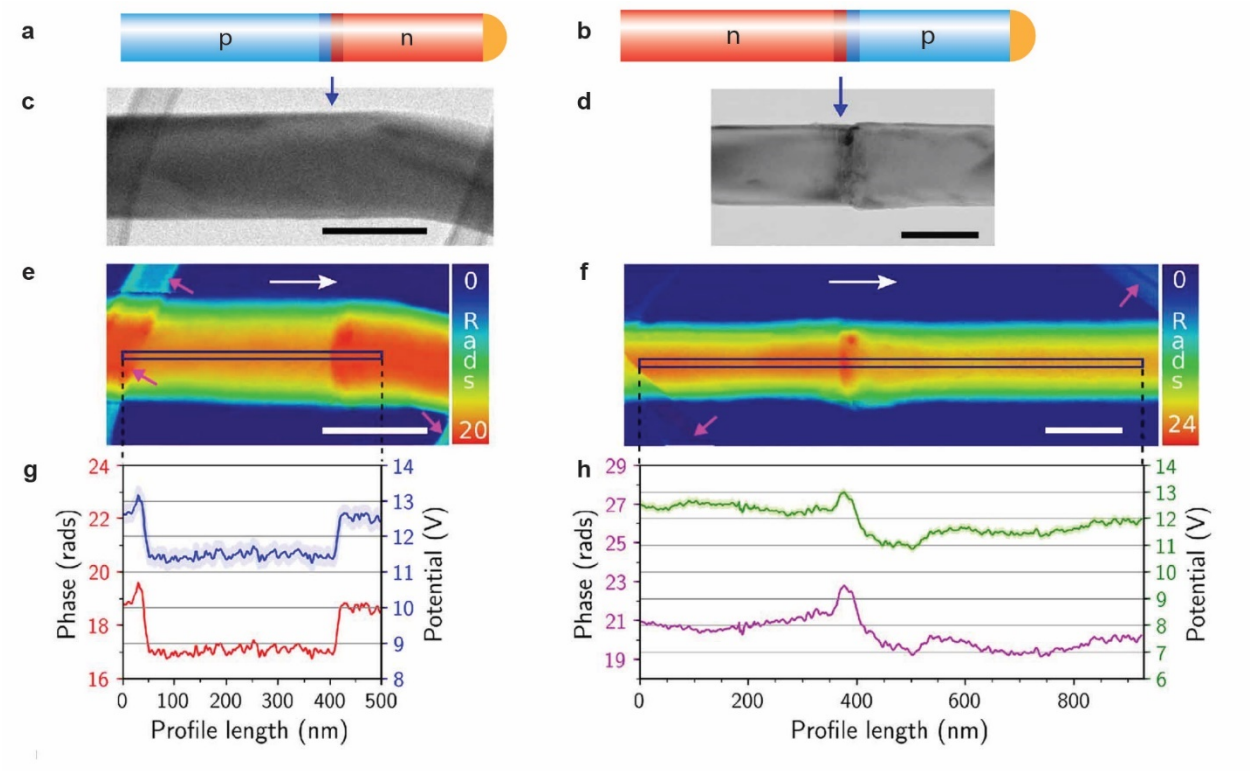

Figure 3.3: EH of Growth 2 tunnel diodes. a, *p-n* and **b**, *n-p* growth 2 sequence schematics (not to scale). **c-d** Bright-field TEM images of the region nearby the p-n junction. Blue arrows indicated the location of the p-n/n-p junction. Scale bars are equal to 200 nm. **e-f,** Pseudo-colored phase images where the white arrows indicate growth direction and fuchsia arrows denote presence of TEM grid. Color bar is in units of radians and scale bars are equal to 200 nm. **g-h** Corresponding 1-dimensional phase and calculated potential profiles taken along the center axis of the NWs as shown by the boxed regions in panels e and f. The blue and green error bands in g and h correspond to the error added by the native oxide on the electron beam direction.

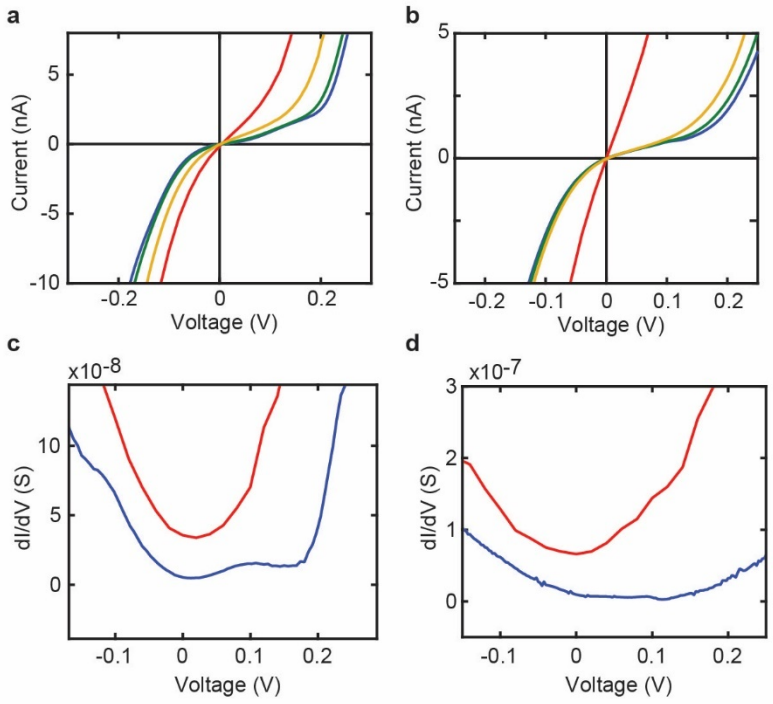

Figure 3.4: Electronic behavior of Growth 1 SiNW tunnel diodes. *I-V* curves Growth 1 tunnel diodes grown in the *p-n* (**a**) and *n-p* (**b**) growth polarity at measurement temperatures of 77 K (blue), 125 K (green), 200 K (yellow) and 298 K (red). **c,** Derivative of the I-V curves at 77 K (blue) and 298 K (red) in panel a. **d,** Derivative of the I-V curves at 77 K (blue) and 298 K (red) in panel b.

To understand the electrical behavior of our SiNW tunnel diodes, we fabricated single NW devices and measured their *I-V* curves at ambient and cryogenic temperatures. Representative *I-V* curves for Growth 1 diodes are shown in Figure 3.4a-b. Neither growth polarities show the expected NDR but both were still very conductive at low biases, suggesting a high current from trap-assisted tunneling that masks the NDR from band-to-band tunneling. By taking measurements at low temperatures down to 77 K, the trap-assisted tunneling is minimized

and the NDR can become more apparent. In the conductance curve for the *p-n* polarity at 77 K, we see a clear inflection point in the forward bias. We do not observe a clear inflection point in the *n-p* conductance curves, however, the *I-V* curves for both growths and the conductance curve in the *p-n* direction closely resembles the *I-V* and conductance curves for Au-doped planar Si tunnel diodes reported in literature[54]. Since band-to-band tunneling has a low probability in indirect bandgap materials[55] and Au-catalyzed wires are known to have some Au-incorporation[77], it is likely that our tunnel diodes conduct via an Au defect-assisted mechanism.

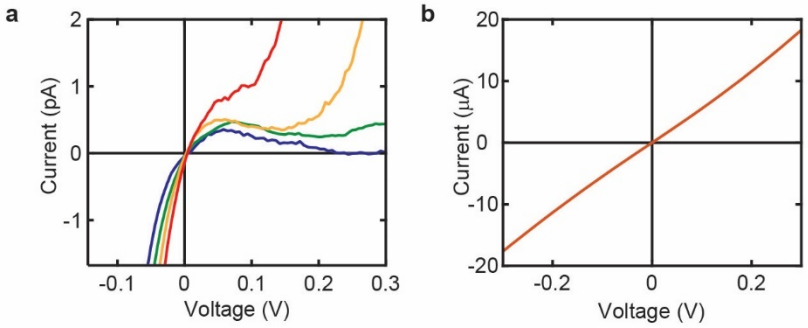

Figure 3.5: Electronic behavior of Growth 2 SiNW tunnel diodes. a, *I-V* curves for a Growth 2 *p-n* diode measured at 77 K (blue), 130 K (green), 200 K (yellow) and 298 K (red). **b,** *I-V* curve for a Growth 2 *n-p* wire measured at 298 K.

The *I-V* curves for Growth 2 are shown in Figure 3.5. For the *p-n* growth polarity, we observed similar *I-V* characteristics as the Growth 1 diodes. For one NW, shown in Figure 3.5a, we observed clear NDR behavior under cryogenic temperatures. For the *n-p* growth polarity, all NWs had a highly conductive and linear *I-V* response.

To compare the conductivities for each growth condition and polarity, we calculated an effective resistance (R_{eff}) which we define as the resistance (R) multiplied by the NW cross sectional area. The resistance was determined from the slope of a linear fit to the low-bias region of room temperature *I-V* curve and the NW radius was measured by SEM. Average values of R and R_{eff} are listed in Table 3.1 alongside the values of V_{bi} and W_D determined by EH. Unexpectedly, the Growth 2 n-p wires had the lowest R_{eff} despite having the longest junction width. Scanning tunneling electron microscopy (STEM) images and elemental mapping with energy dispersive x-ray spectroscopy (EDS), shown in Figure 3.6 a-b, revealed that this growth condition induces a large gold deposition at the junction. Integration of the Au signal across the radius of the wire (Figure 3.6 c) results in an Au signal that is roughly uniform across the radius, unlike the Si signal which increases through the center of the wire, suggesting that most of the Au is on the surface of the wire. The integration of the Au signal along the NW axis shows that this deposition is localized to the junction where the dopants are switched.

Table 3.1: Summary of SiNW tunnel diode metrics

		V_{bi} (V)	W_D (nm)	R(MΩ)	R_{eff} (mΩ*cm^2)
Growth 1	*p-n*	1.17 ± 0.02	19 ± 2	18.2	6.1 ±6.3
	n-p	0.86 ± 0.01	12 ± 1	8.25	2.7 ± 8.9
Growth 2	*p-n*	1.02 ± 0.02	10 ± 1	4041.6	1300 ± 800
	n-p	0.8 ± 0.3	77 ± 20	0.013	0.0061± 0.0035

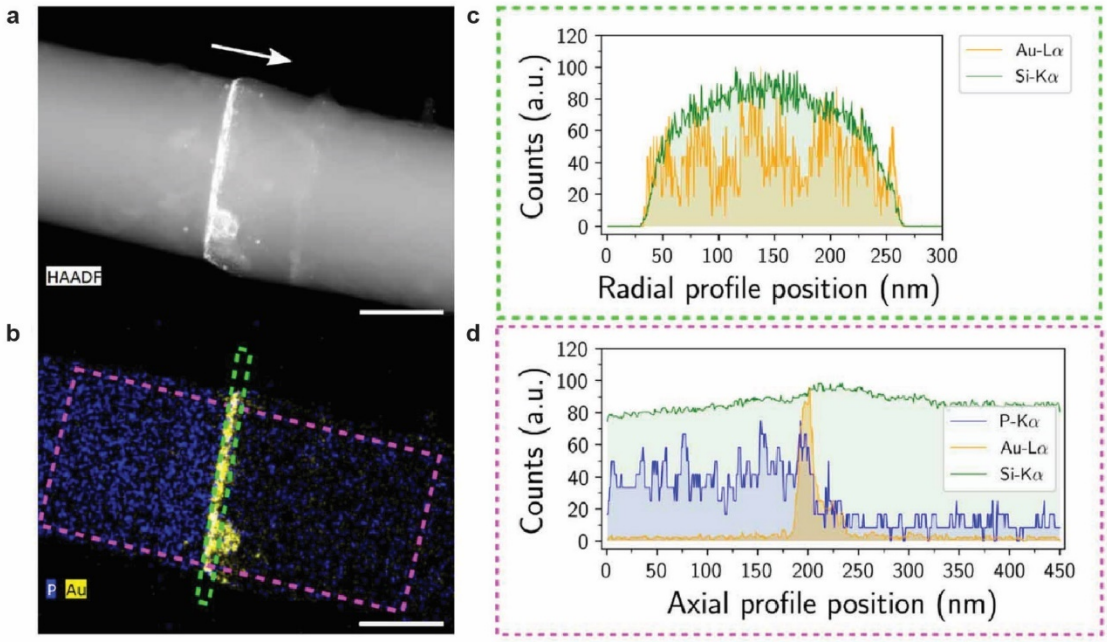

Figure 3.6: STEM imaging of Growth 2 n-p wire. a, HAADF image of the junction of a Growth 2 n-p wire. Arrow indicates growth direction. Scale bar, 100 nm. **b**, EDS map of P and Au for the image in panel a. Scale bar, 100 nm. **c,** Au and Si EDS counts as a function of radial profile position taken along the green box in panel b. **d**, Si, Au and P EDS counts as a function of axial profile position taken along the fuchsia box in panel b.

While the average R_{eff} for both Growth 1 conditions is smaller than the Growth 2 p-n condition, there were large variations in R and R_{eff} between wires within the same growth conditions. This agrees with our hypothesis that the main conduction mechanism is defect-assisted tunneling through mid-gap Au traps, a quantity that we cannot control precisely. Based on the low R_{eff} of the Growth 2 *n-p* junctions, they would seem optimal for our MJ SiNW

devices. However, since the gold deposition is likely a result of catalyst instability,[73] there was often a kink at the junction which is not desirable for our MJ structures.

3.2.2 SiNW Multijunction Photovoltaic Devices

SiNWs ~150-200 nm in diameter were also grown by a Au-catalyzed VLS process in a home-built CVD reactor. During growth, the SiNWs were sequentially encoded with a variable number (N) of *p-i-n* or *n-i-p* units, giving similar results for both growth polarities. An example $N = 10$ *n-i-p* SiNW is shown by the scanning electron microscopy (SEM) image in Figure 3.7a, and the presence of the *n-i-p* superlattice was verified by infrared scattering-type scanning near-field optical microscopy (s-SNOM), which can directly map free carrier concentration along the length of a single SiNW[47,62]. As indicated by the contrast in the s-SNOM image in Figure 3.7b, individual *n-i-p* units are clearly distinguishable along the length of the SiNW, verifying the fidelity and uniformity of the encoded structure.

The PV performance of individual *n-i-p* units were characterized by fabricating metallic contacts to each junction of an $N = 5$ SiNW after selective wet-chemical etching to reveal the junction location, as shown by the SEM images in Figure 3.7c. *I-V* characteristics measured from each junction (labeled by junction index j) under 1-sun illumination are shown in Figure 3.7d with PV metrics (I_{SC}, V_{OC}, FF), series resistance (R_S), I_o, n, and surface recombination velocity (S)) collected in Table 3.2. Although the etching causes variations in I_{SC} and I_o, the V_{OC}, FF, n, and S are comparable to one another and to single junctions reported in the literature[46,47], verifying the high quality of individual junctions. *I-V* curves measured across an increasing number of *n-i-p* units (Figure 3.7e) exhibit a V_{OC} that is additive and an I_{SC} that is, as expected, limited by the lowest I_{SC} in the series.

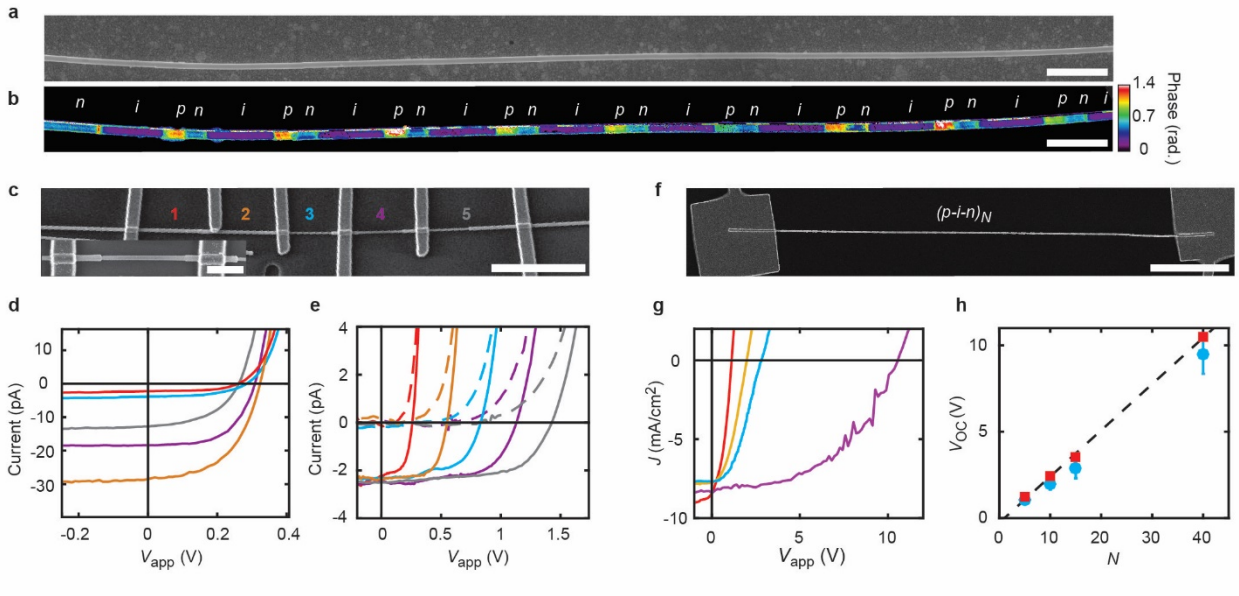

Figure 3.7: Single MJ SiNW PV devices. a, Composite SEM image of an $N = 10$ *n-i-p* SiNW; scale bar, 2 μm. **b**, s-SNOM phase map of the SiNW shown in panel a with individual *p*-type (*p*), intrinsic (*i*) and *n*-type (*n*) segments labeled; scale bar, 2 μm. **c**, SEM image of an etched $N = 5$ *n-i-p* SiNW with contacts defined for each junction labeled 1-5; scale bar, 5 μm. Inset: higher magnification SEM image showing junction 4; scale bar, 1 μm. **d**, *I-V* curves under 1-sun illumination of junction 1 (red), 2 (orange), 3 (cyan), 4 (violet), and 5 (gray). **e**, *I-V* curves from the same device as panel d measuring across junction 1 (red) and junctions 1 through 2 (orange), 3 (cyan), 4 (violet), and 5 (gray). Dashed and solid lines were collected in the dark and under 1-sun illumination, respectively. **f**, SEM image of an unetched $N = 15$ *p-i-n* SiNW with contacts on the *n*- and *p*-type terminals; scale bar, 10 μm. **g**, *I-V* curves for $N = 5$ (red), 10 (orange), 15 (cyan), and 40 (violet) SiNW devices under 1-sun illumination. **h**, Average (cyan circles) and champion (red squares) V_{OC} as a function of N. Dashed line represents a linear fit to champion devices.

Table 3.2: PV metrics for individual *n-i-p* junctions in a $N = 5$ SiNW

junction index (j)	L_i (μm)	D_i (nm)[a]	I_{SC} (pA)	V_{OC} (V)	FF	R_S (GΩ)	I_o (fA)	n	S (cm/s)[b]
1	2.1	180	2.2	0.25	0.58	18	15	2.0	1.04E+03
2	2.1	163	28.4	0.32	0.53	2.3	32	2.0	2.46E+03
3	2.1	93	3.9	0.28	0.52	14	8.3	1.9	1.12E+03
4	2.1	120	18.3	0.30	0.60	23	58	2.1	6.11E+03
5	2.1	114	12.6	0.25	0.50	4.1	18.5	2.1	2.03E+03

[a]diameter of etched intrinsic segment

The PV performance of *p-i-n* and *n-i-p* superlattices was tested by fabricating single SiNW devices with electrical contacts on the n-type and p-type end segments (Figure 3.3f), enabling measurement under an applied voltage (V_{app}) across all synthetically encoded PV junctions and tunnel junctions. Figure 3.7g shows current density-voltage (*J-V*) curves, where *J* is defined by using the projected area of the intrinsic segment, under 1-sun illumination for champion SiNW devices with $N = 5$, 10, 15, and 40, L_i's of 2.1, 2.1, 1.5, and 0.2 μm, and n-type/p-type segments lengths of 1.3, 1.3, 1.3, and 0.2 μm, respectively. Note that the length of individual *p-i-n* units was reduced for higher *N* to reduce the total length of the SiNWs and facilitate device fabrication, and $N = 5$, 10 and $N = 15$, 40 Si NWs were grown in *n-i-p* and *p-i-n* sequences, respectively. We estimate the overall IQE to be ~60% from each junction in our champion devices, which agrees well with a spatially-dependent IQE of near unity in the intrinsic regions and near zero in the p- and n-type regions, as predicted by device simulations[47]. This highlights the potential to improve overall performance in the future through minimization of the n-type and p-type segment lengths where carrier collection efficiency is low.

All PV metrics are summarized in Table 3.3, allowing us to observe trends as we change

N. As *N* increases, the value of J_{SC} is approximately constant while V_{OC} increases linearly, as shown in Figure 3.7h, highlighting the consistency of junctions within individual SiNWs and consistency between the *n-i-p* and *p-i-n* growth polarities. A linear fit to champion devices yields a value of 0.27 V/junction (Figure 3.7h), which is consistent with V_{OC} measurements on single junctions. Notably, a SiNW with $N = 40$ yielded a V_{OC} above 10 V, which is in substantial excess of the voltage needed for water splitting. R_S also increased linearly with *N*, and the increase (~8 MΩ/junction) is consistent with the effective resistance of a tunnel junction[74]. *n* also increases linearly with the number of junctions, which is consistent with the ideal diode equation.

Table 3.3: Single MJ SiNW PV metrics

N	Growth Polarity	D^a (nm)	L_i (μm)	V_{OC} (V)	V_{OC}/N (V/junc.)	I_{SC} (pA)	*FF*	R_S/N (GΩ/junc)	I_o (fA)	*n/N*	*S* (cm/s)
5	*n-i-p*	200	2.1	1.23	0.25	23.9	0.37	2.04	184	1.68	1.15E+04
				1.06	0.21	21.7	0.31	17.5	77	1.09	4.82E+03
				0.98	0.20	19.4	0.39	3.43	66	1.28	4.11E+03
				0.89	0.18	14.4	0.54	4.86	423	1.08	2.65E+04
				0.89	0.18	21.1	0.41	9.12	41	0.83	2.55E+03
10	*n-i-p*	200	2.1	2.43	0.24	13.2	0.43	14.3	145	1.76	9.10E+03
				2.35	0.24	12.1	0.44	7.45	367	2.37	2.30E+04
				2.27	0.23	14.9	0.49	4.16	319	1.65	2.00E+04
				2.21	0.22	16.0	0.42	16.6	469	1.87	2.94E+04
				2.18	0.22	18.7	0.36	15.5	60	1.66	3.73E+03
				2.18	0.22	25.0	0.39	10.3	274	1.72	1.72E+04
				2.16	0.22	11.8	0.42	9.56	159	1.64	9.98E+03
				2.12	0.21	31.7	0.42	6.39	223	1.29	1.39E+04
				2.07	0.21	20.7	0.31	13.0	76	1.11	4.77E+03
				2.03	0.20	27.0	0.36	5.61	879	2.11	5.50E+04
				2.00	0.20	33.1	0.36	2.67	259	1.61	1.62E+04
				2.00	0.20	12.9	0.55	2.28	491	1.64	3.08E+04
				1.92	0.19	24.4	0.33	6.16	294	1.53	1.84E+04
				1.89	0.19	16.1	0.37	14.0	348	1.64	2.18E+04
				1.80	0.18	18.3	0.48	5.79	55	0.83	3.42E+03
				1.79	0.18	6.3	0.37	21.3	113	0.97	7.11E+03
				1.74	0.17	24.9	0.44	3.32	451	1.19	2.83E+04
				1.68	0.17	29.9	0.37	4.71	1750	1.57	1.10E+05
				1.62	0.16	16.5	0.42	0.52	2330	1.80	1.46E+05
				1.52	0.15	19.3	0.27	1.63	170	0.93	1.06E+04
				1.48	0.15	40.0	0.44	0.46	207	0.85	1.30E+04
				1.31	0.13	5.5	0.32	13.5	566	1.90	3.55E+04

Table 3.3: Single MJ SiNW PV metrics (continued)

N	Growth Polarity	*D*[a] (nm)	L_i (µm)	V_{OC} (V)	V_{OC}/N (V/junc.)	I_{SC} (pA)	*FF*	R_S/N (*G*Ω/junc)	I_o (fA)	*n/N*	*S* (cm/s)
15	*p-i-n*	200	1.5	**3.49**	**0.23**	**5.0**	**0.56**	**16.3**	**79**	**2.00**	**6.89E+03**
				3.19	0.21	13.8	0.35	16.5	51	1.74	4.49E+03
				3.02	0.20	6.1	0.49	11.5	116	1.47	1.01E+04
				2.81	0.19	22.5	0.4	17.2	5.67	1.08	4.97E+02
				2.6	0.17	8.2	0.35	24.4	0.56	1.02	4.06E+01
				1.94	0.13	5.8	0.46	15.0	48	1.05	4.20E+03
40	*p-i-n*	150	0.2	10.5	0.26	2.2	0.49	19.9	5.62	1.56	4.93E+03
				10.2	0.26	2.0	0.85	53.4	1.80	1.19	1.58E+03
				10.1	0.25	1.1	0.67	29.6	5.74	2.03	5.03E+03
				9.62	0.24	1.6	0.47	62.0	1.22	1.26	1.07E+03
				8.4	0.21	4.4	0.52	11.4	45	1.06	3.98E+04
				7.81	0.20	1.4	0.53	35.7	9.68	1.41	8.49E+03

[a] approximate diameter of catalyst used

Previous studies of single junction *p-i-n* wires show an increase in device performance after a brief thermal oxidation and an anneal in H_2 gas[47]. A thermal oxidation is incompatible with our MJ SiNWs because the diffusion of B and P in Si is significant at the temperatures required for a thermal oxidation (>900 °C), ruining the tunnel junctions. Therefore, all wires shown in Table 3.3 underwent a hydrogen anneal only. Figure 3.8 shows the effect of the H_2 anneal on *N*= 5 and 10 wires grown in the *n-i-p* direction. The anneal greatly improves the quality of the diode and annealed wires have much higher I_{SC} and *FF* than the unannealed wires.

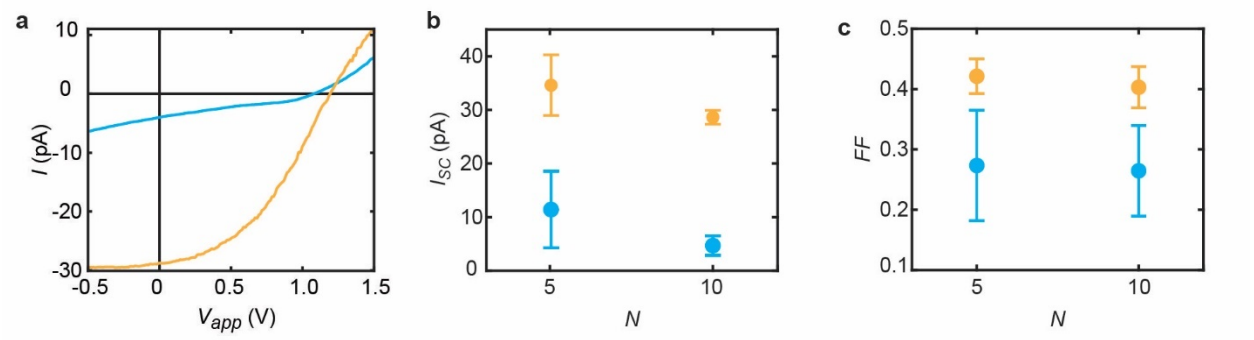

Figure 3.8: Effect of hydrogen anneal on PV performance: a, *I-V* curves for $N = 5$ *n-i-p* SiNW PV devices with an anneal (yellow) and without an anneal (cyan) under 1-sun illumination. **b**, I_{SC} **c,** and *FF* $N = 5$ and 10 *n-i-p* PV devices with an anneal (yellow) and without an anneal (cyan).

With increasing illumination intensities, the SiNWs exhibited a linear increase in I_{SC} and logarithmic increase in V_{OC} (Figure 3.9 a-b), as expected for PV devices behaving according to the ideal diode equation, and demonstrated that our tunnel junctions are capable of facilitating a high photocurrent. I_o and n can be determined by either fitting the dark curve to the ideal diode equation or by a linear fit to a semi-log plot of I_{SC} and V_{OC} and both methods have previously been shown to agree with each other[64,78]. However, when using both these strategies on our MJ SiNWs, we get different values. A fit of the dark *I-V* curve to a modified diode equation that includes R_S (for simplicity, we assume $R_{Sh} \sim \infty$), shown in Figure 3.9c, results in a normalized ideality factor (n/N), I_o, and R_S of 1.53, 234 fA, and 36 GΩ, respectively. The semi-log plot of I_{SC} and V_{OC} is shown in Figure 3.9d and a linear fit of the data yields a n/N of 1.27 and I_o 51 fA. The semi-log plot method does not account for the effect of parasitic resistances, which could be causing this discrepancy[64]. All I_o values shown in Table 3.3 were calculated using a fit to the dark *I-V*.

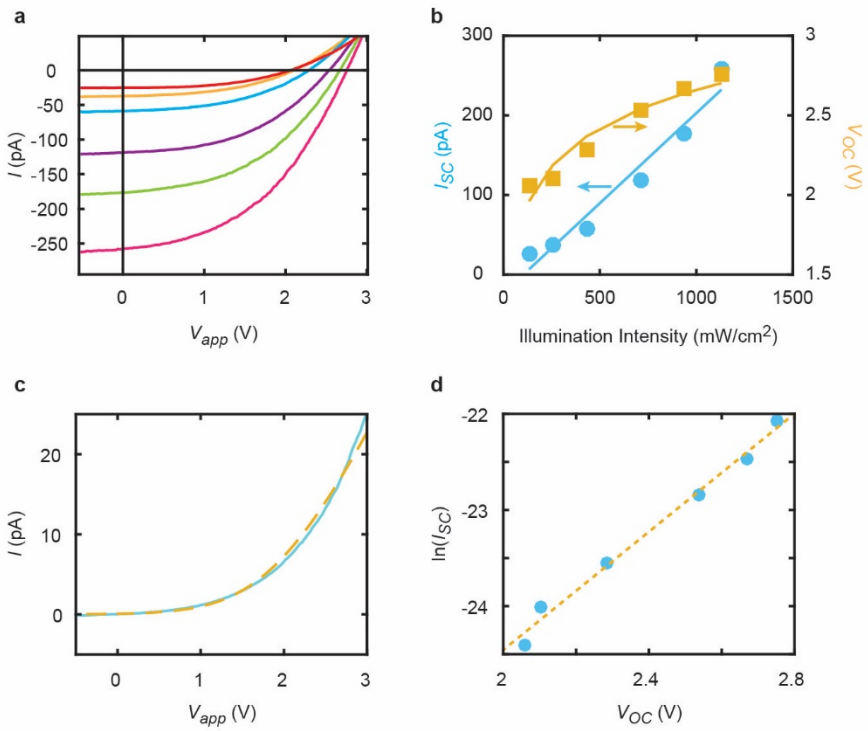

Figure 3.9: Single $N = 10$ *n-i-p* SiNW PV device under multi-sun illumination. a, The *I-V* curves of a $N = 10$ SiNW under 1.3 sun (red), 2.5-sun (orange), 4.3-sun (cyan), 7.2-sun (purple), 9.4-sun (green), and 11.3-sun (magenta) illumination. **b**, The dependence of I_{SC} (cyan) and V_{OC} (orange) on the illumination intensity for the SiNW shown in panel a. Solid lines show the linear fit (cyan) and logarithmic fit (orange) for the I_{SC} and V_{OC} trends, respectively. **c**, Dark *I-V* curve (cyan) of the same SiNW with a fit to the ideal diode equation modified to include R_S (yellow, dashed). **d**, Plot of ln(I_{SC}) vs. V_{OC} from the multi-sun illumination data shown in panels a-b with a linear fit (dashed).

3.3 Conclusions

Using precise control of the VLS growth mechanism, we were able to synthesize VLS-grown SiNW tunnel junctions for the first time and realize MJ SiNWs with an unlimited number of junctions. Increasing the number of junctions in series results in a linearly increasing V_{OC} with

minimal impact to other device metrics such as I_{SC} and FF, allowing for a tunable high-voltage PV device. In the future, measurements on tunnel junction devices at. liquid helium temperatures (4.2K) could lower the excess current enough to observe band-to-band tunneling and perhaps even phonon modes. For the MJ PV devices, a more rigorous study of the geometric parameters not explored here (e.g. length of the n and p-type segments) and alternative surface treatments could yield a higher efficiency device. Additionally, scanning photocurrent microscopy of MJ SiNW structures could be used to measure the spatially-resolved photocurrent to measure a spatially dependent IQE and better understand the photocurrent enhancement in the H_2 annealed wires[48,79].

3.4 Acknowledgments

Electron holography data was collected and analyzed by Dr. Cristina Cordoba and Dr. Karen Kavanagh at Simon Fraser University. s-SNOM measurements and map were done by Earl Ritchie and Dr. Joanna Atkin at University of North Carolina at Chapel Hill. This work was performed in part at the Chapel Hill Analytical and Nanofabrication Laboratory, CHANL, a member of the North Carolina Research Triangle Nanotechnology Network, RTNN, which is supported by the National Science Foundation, Grant ECCS-2025064, as part of the National Nanotechnology Coordinated Infrastructure, NNCI.

CHAPTER 4: PHOTOELECTRODEPOSITION OF WATER-SPLITTING CO-CATALYSTS

4.1 Introduction

After the electrons and holes are successfully separated in a photocatalyst particle, they must react with the water molecules and protons in solution, and this charge transfer step creates an additional energy barrier beyond the thermodynamic energy cost of 1.23 V. For an efficient reaction, a co-catalyst is needed to facilitate the charge transfer and lower the kinetic energy barrier for the reaction. (Figure 4.1) In the case of silicon, this is especially true due to the electrically insulating native oxide layer that forms on the surface. The best co-catalysts are often efficient electrocatalysts, which have been studied extensively to illuminate the relationship between catalyst performance and the reaction mechanism.

For the hydrogen reduction reaction, the best co-catalysts have a zero net energy of adsorption (ΔG_{ads}) between the catalyst and hydrogen atoms, allowing both adsorption of protons and desorption of H_2[80]. Experimentally, the best materials for the HER are noble metals such as platinum (Pt), palladium (Pd) and rhodium (Rh)[25,81]. Water oxidation is a more complex multi-step reaction that is kinetically slower. Theoretical studies on the adsorption energies of the water oxidation reaction intermediates showed that the best materials for catalyzing the OER are those that have a $\Delta G_{O*} - \Delta G_{HO*} \sim 1.5$ eV[82], where ΔG_{O*} and ΔG_{HO*} are the adsorption energies of oxygen and hydroxyl groups respectively. The lowest reported overpotentials for the OER are for metal oxide materials, with IrO_x, CoO_x, RuO_x and NiO_x being the top choices[25,83].

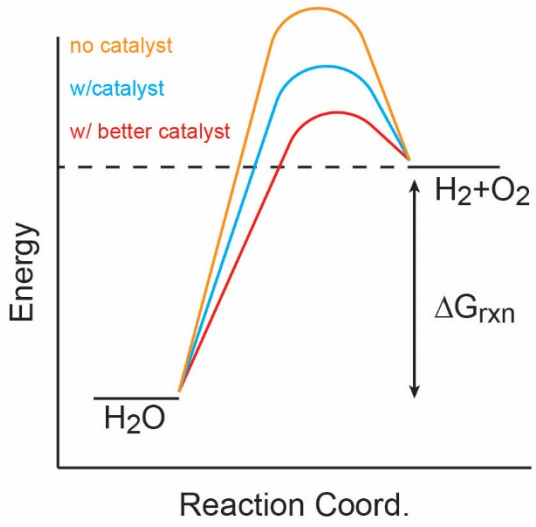

Figure 4.1: Energy Diagram of water splitting reaction: The kinetic overpotential of the water splitting reaction can be decreased with efficient catalyst incorporation.

Additional concerns when designing the co-catalyst are selectivity for the desired half reaction, catalyst loading amount, and catalyst loading location. Many of the best proton reduction catalysts, including Pt, will also readily reduce oxygen to form H_2O [84]. One strategy to combat this is depositing a thin layer of material on the outside of the HER co-catalyst that is permeable to H^+ and H_2 but not O_2 or H_2O [85], such as Cr_2O_3[86]. When loading the co-catalyst materials, there is an optimal amount where there are sufficient catalytic sites but the deposition is not too thick. Excessive co-catalyst deposition can block light to the semiconductor, introduce too many charge recombination centers, or lose catalytic activity by becoming a large bulk particle[87]. Location of the deposition can also affect performance and, as seen in CdS nanorods[88,89] and $BiVO_4$ platelets[90], spatially-separated deposition of the HER and OER catalysts can improve photocatalytic performance by minimizing charge recombination. Common

methods for co-catalyst loading include impregnation, photodeposition, chemical reduction, sol-gel, precipitation, and hydrothermal techniques[87].

The ideal co-catalyst design for our MJ SiNW photocatalysts would be a thin layer of noble metal on the n-type end and a thin layer of metal oxide on the p-type end, with no deposition on junctions in between. While this initially seems like a challenging synthesis, the inherent electrical asymmetry makes it a perfect candidate for spatioselective photodeposition. Under illumination, the asymmetric potential generated across the structure can be used to drive reduction or oxidation of metal ions in solution.

4.1.1 Photodeposition

Unlike planar photoelectrodes that can be easily dipped into solutions, loaded into physical vapor deposition chambers, or biased for electrodepositions, particulate photocatalysts must generally be functionalized with co-catalysts in solution. Since the particles are already photoelectrochemically active, photodeposition has become a common method to deposit metal and metal oxide co-catalysts for the HER and OER respectively. In order for a photodeposition to occur, the semiconductor valence and conduction bands must straddle the redox potential of the metal ion species[91]. The electron-hole pairs generated under illumination can reduce and oxidize metal ions in species to form metals and metal oxides, respectively (Figure 4.2a).

Photodeposition is not inherently spatioselective and in most cases the metal or metal oxide is deposited randomly on the surface. In a few literature examples, the light-absorbing particle has been engineered to induce spatial selectivity. For example, facet-engineered $BiVO_4$ platelets[90] can produce a built-in electric field that drives electrons and holes towards different facets[92]. There are also several examples of *p-n* junction assisted catalyst deposition, where the

built-in potential induces selective reduction in the *n*-type region and oxidation in the *p*-type region (Figure 4.2b)[93]. For the silicon nanowire photocatalysts, it is vital to limit co-catalyst deposition to the nanowire ends, since deposition on the junction area could result in electrically shorting or optically shadowing the junctions.

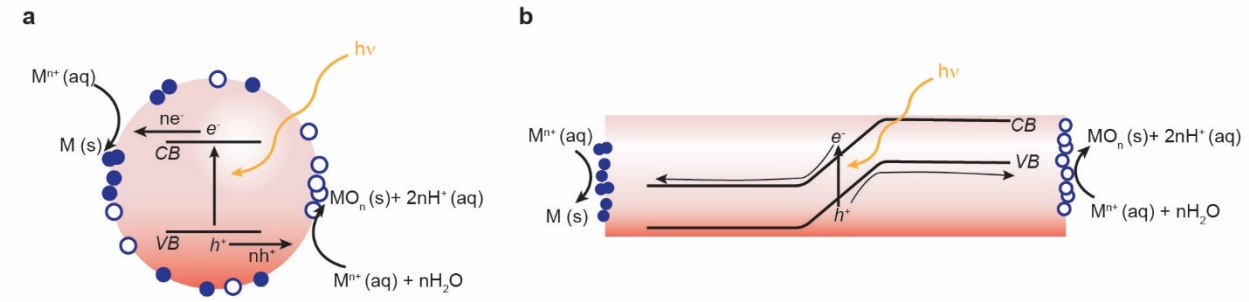

Figure 4.2: Photodeposition process. a. Diagram of photodeposition on a semiconductor material, where electrons and holes generated under illumination may diffuse to the surface and react and reduce or oxidize metal ions in solution. **b.** Photodeposition at a *p-n* junction, where the built-in potential sweeps carriers to opposite ends of the material, resulting in a spatioselective deposition.

4.2 Results and Discussion

We developed a bottom-up spatioselective photoelectrodeposition process utilizing the built-in potential to electrochemically deposit a metal or metal oxide at the ends of the SiNWs, using Pt and cobalt oxide (CoO_x) materials as the HEC and OEC, respectively. Pt deposition was optimized on *n*-type terminated *p-i-n* superlattices by immersing in an aqueous solution containing 5 mM $[PtCl_6]^{2-}$ for 10 min under 5-sun illumination, which resulted in reduction to

form Pt on the Au tip, as shown by the transmission electron microscopy (TEM) image and scanning transmission electron microscopy (STEM) energy dispersive x-ray spectroscopy (EDS) elemental map in Figure 4.3a. CoO_x deposition was optimized on *p*-type terminated *n*-*i*-*p* superlattices by immersing in an aqueous solution of 5 mM Co^{2+} for 3 min under 5-sun illumination, resulting in oxidation to form CoO_x on the Au tip (Figure 4.3b). The individual maps of each element (Figure 4.3c-d) show that both catalyst materials preferentially deposit on the gold catalyst tip, rather than the wire itself, likely due to a lower overpotential of charge transfer at the metal-solution interface. The oxygen signal seen in the Pt deposition is primarily background signal and there is only very weak oxygen peak when integrating the signal over the catalyst area (Figure 4.3e).

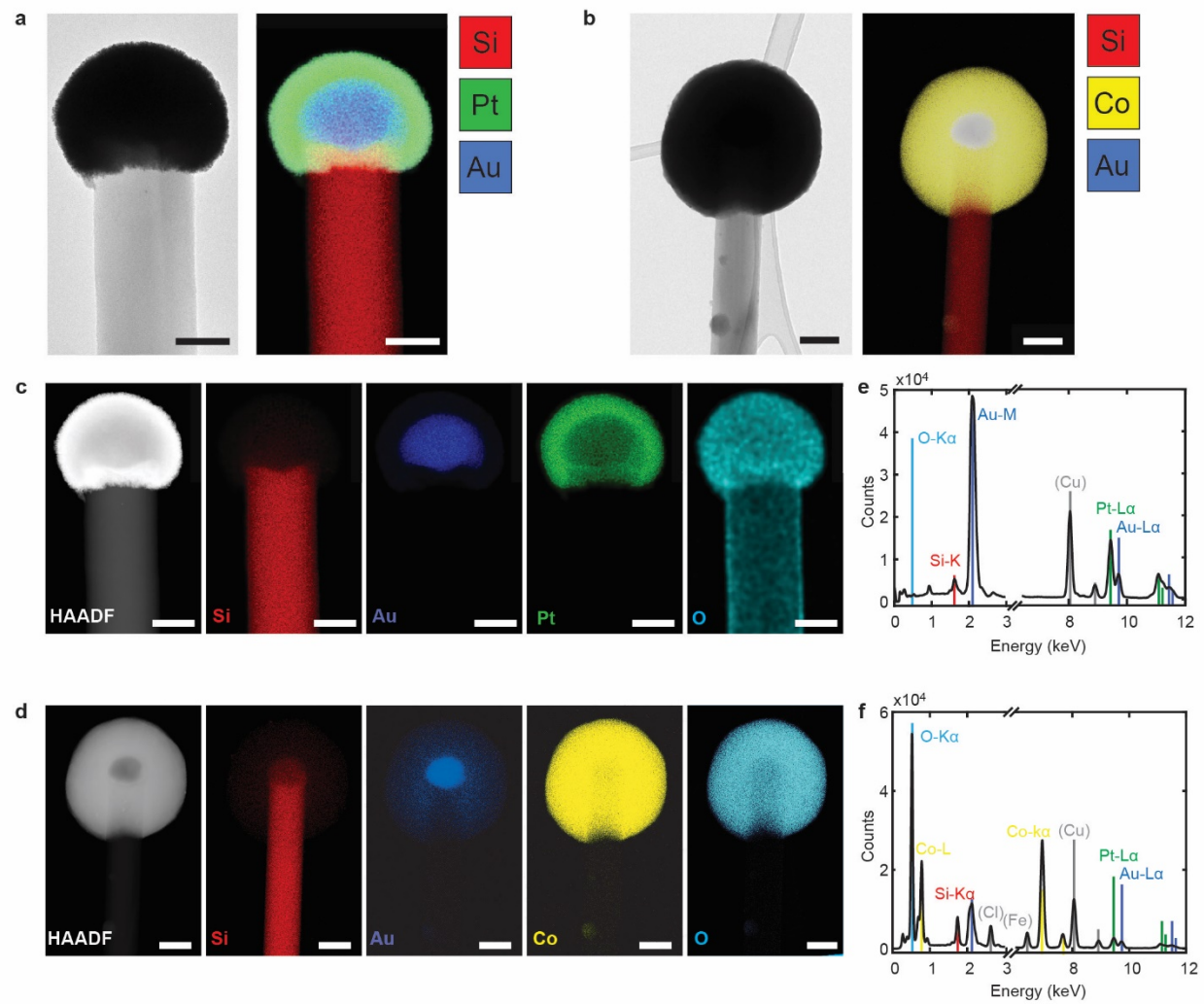

Figure 4.3: Photodeposition of Pt and CoOx: a-b, HRTEM image (left) and color-coded STEM EDS elemental map (right) for Pt deposited on a *p-i-n* superlattice (panel a) and CoO_x deposited on an *n-i-p* superlattice (panel b). scale bars, 100 nm for panel a and 200 nm for panel b. **c-d,** STEM high-angle annular dark field (HAADF) images (far left) and color-coded EDS maps (right) of individual elements for the depositions in scale bars, 100 nm for panel c and 200 nm for panel d. **e-f,** Integrated EDS signal spectrum over the catalyst area with major peaks labelled.

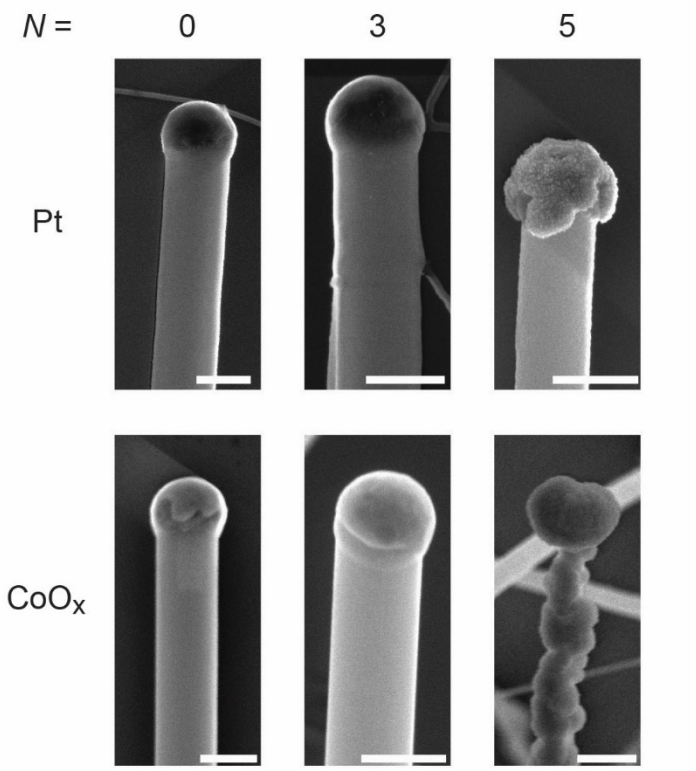

Figure 4.4: Junction dependence of photodeposition process. SEM images of Pt and CoO_x deposition on SiNWs with different number of encoded junctions, *N*. Wires with zero junctions were n-type (Pt deposition) or p-type (CoO_x) doped only. All scale bars equal to 200 nm except for bottom right image, which is 500 nm.

The same deposition process was attempted on wires with fewer junctions but no material deposition was observed on SiNWs with less than 5 junctions (Figure 4.4), which suggests that the photodeposition process requires a minimum photovoltage to drive the reaction. Based on the known photovoltages of *N*=5 MJ SiNW PVs, this puts the minimum voltage for Pt and CoO_x deposition at around 1 V, although the illumination conditions during our deposition are rather different and could result in a different voltage generation.

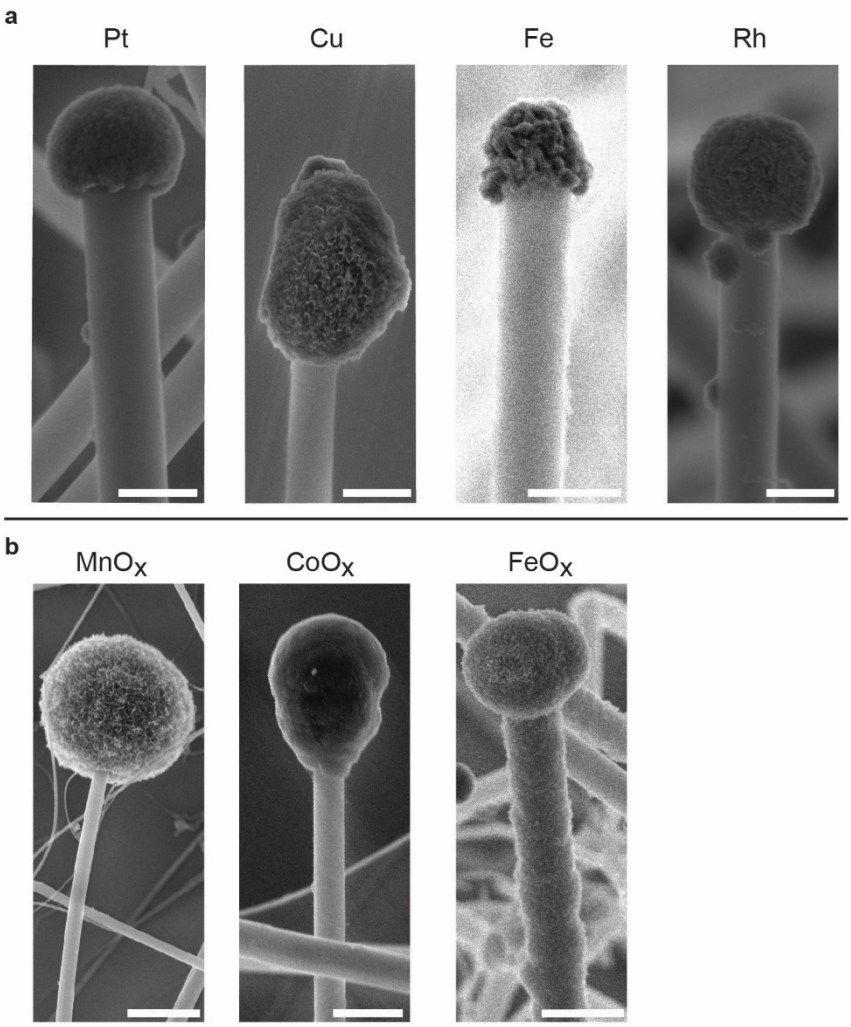

Figure 4.5: Gallery of photodeposited materials. SEM images of materials deposited onto N = 15 wires via **a**, photoreduction onto *p-i-n* wires or **b,** photooxidation onto *n-i-p* wires. Scale bars in panel a are equal to 200 nm. Scale bars in panel b are equal to 1µm, 500 nm, and 500 nm (left to right).

This photodeposition process can be used to deposit several metal and metal oxide materials in addition to CoO_x and Pt, shown in Figure 4.5. Precursors for these depositions are listed in Table 2.1. Interestingly, Fe^{3+} could be photoreduced to deposit Fe, but reduction of Fe^{2+} was unsuccessful, which could be due to its more negative reduction potential. Since the metal

Au tip of our SiNWs should equilibrate to the redox potential of the metal, the half reaction occurring at the base should govern the thermodynamic favorability of our deposition reaction. No sacrificial reagents were used in any of the depositions, so we hypothesize that the base of the wire must either be oxidizing/reducing the silicon, H_2O, or dissolved gases in solution. In the future, use of sacrificial reagents could unlock more negative reduction reactions and more positive oxidation reactions to increase the number of available co-catalyst materials.

In order to achieve co-functionalization of HER and OER co-catalysts onto the same SiNW, the photoreduction and photooxidation processes were combined as a two-step sequence on *p*-*i*-*n* superlattices (Figure 4.6) by first depositing Pt on the Au tip, releasing SiNWs from the silicon oxide growth substrate by sonication, and then depositing CoO_x as a conformal shell on the *p*-type base of SiNWs suspended in solution. High-resolution transmission electron microscopy (HRTEM) images in Figure 4.6b and STEM EDS maps in Figure 4.6c confirm the spatioselectivity of the two processes, with EDS spectra showing no evidence of Pt at the *p*-type base (Figure 4.6d) or Co at the *n*-type tip (Figure 4.6d). This opposite deposition order was attempted but we found that Pt did not reliably deposit on the *n*-type base of the *n*-*i*-*p* structures (Figure 4.7). Additional HRTEM shows that the Pt is nanocrystalline while the CoO_x is amorphous (Figure 4.8)

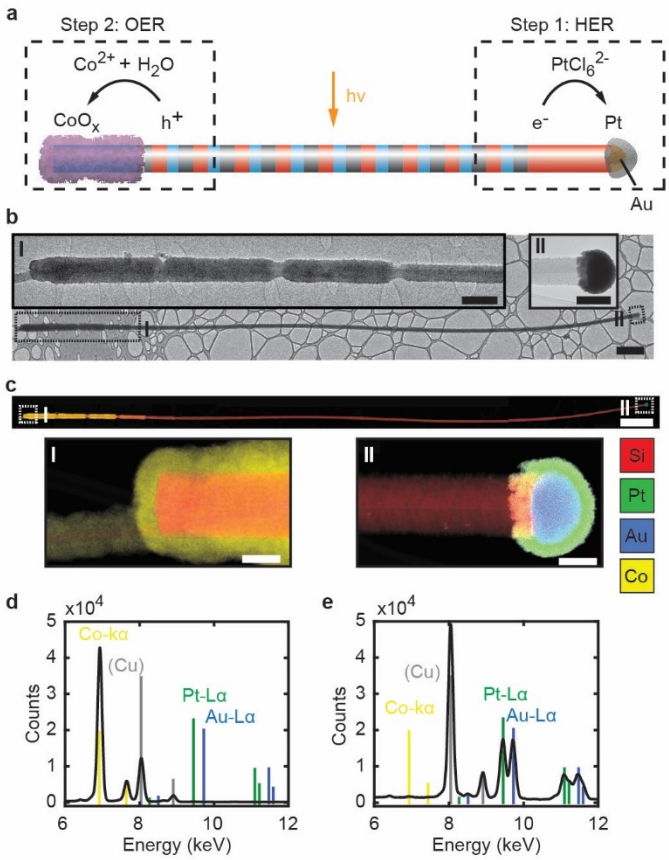

Figure 4.6: Spatioselective photodeposition on MJ *p-i-n* wires a, Schematic illustrating the sequential photodeposition. **b,** HRTEM image of an $N = 15$ *p-i-n* SiNW with Pt and CoO_x deposition; scale bar, 2 μm. Insets: higher magnification images of the *p*-type base (I) and *n*-type tip (II); scale bars, 600 nm (I) and 200 nm (II). **c**, Upper: Composite STEM EDS elemental map of the SiNW shown in panel d; scale bar, 2 μm. Lower: higher magnification maps of the boxed regions labeled I and II; scale bars, 100 nm. **d-e**, EDS spectra (black lines) from the p-type base (panel f) and n-type tip (panel g) of the SiNW. Colored lines show the expected peak positions of Co (yellow), Pt (green), Au (blue), and Cu (gray). Cu signals originate from the HRTEM grid.

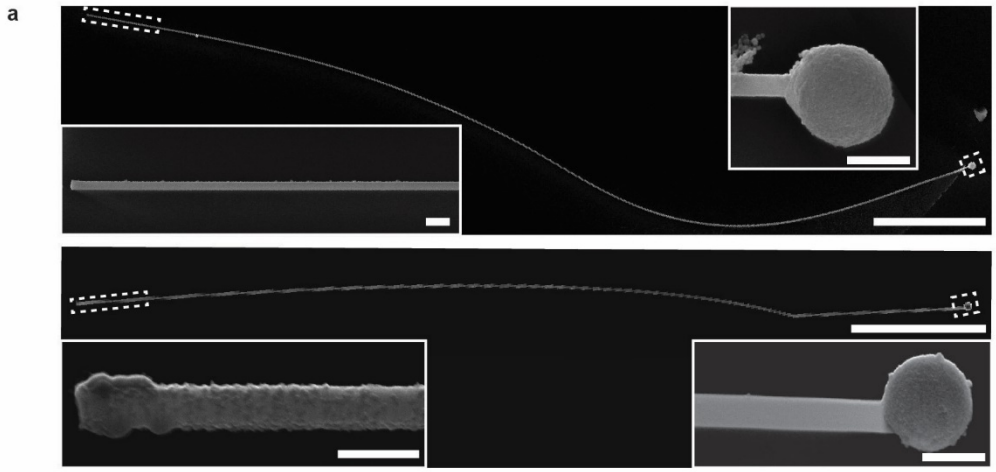

Figure 4.7: Sequential deposition on MJ *n-i-p* wires: a, SEM images of two co-functionalized *n-i-p* SiNWs; scale bars, 5 μm. Insets: higher magnification images of the dashed boxed regions showing the *n*-type bases with Pt (left) and *p*-type tips with CoO_x (right); scale bars, 200 nm. Pt deposition was only evident on the *n*-type base of a fraction of the SiNWs, and the amount of deposited material was small compared to CoO_x deposition on the *p*-type base of *p-i-n* SiNWs.

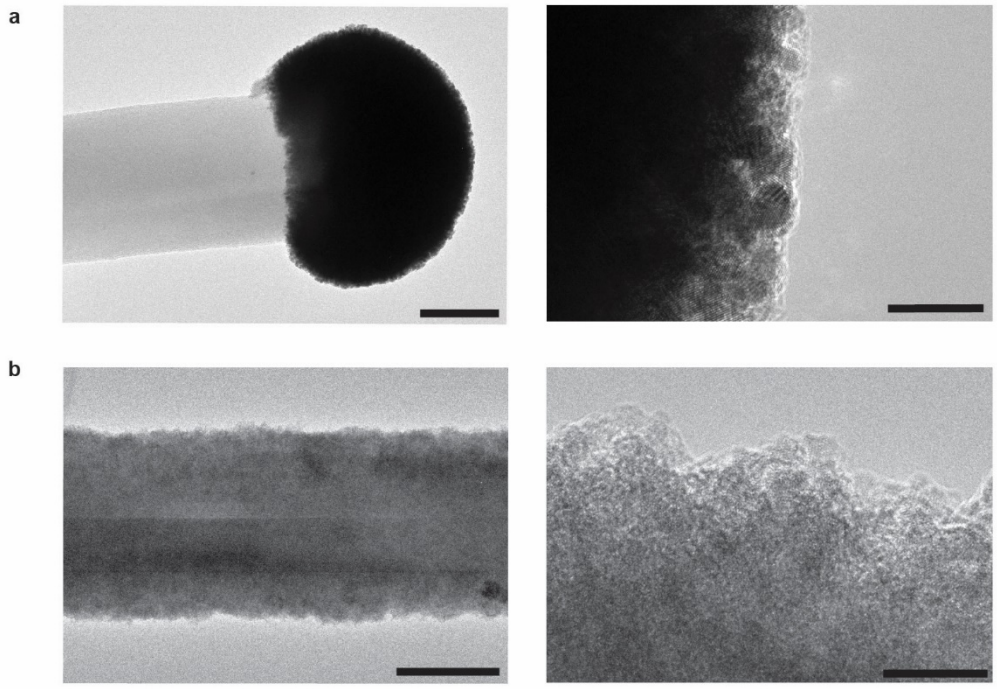

Figure 4.8 HRTEM of sequentially deposited catalysts: a, TEM images of the Pt-functionalized *n*-type tip of a *p*-*i*-*n* SiNW at low magnification (left) and higher magnification (right), showing the polycrystalline nature of the deposited Pt nanoparticles; scale bars, 100 nm (left) and 10 nm (right). **b**, TEM images of the CoO_x functionalized *p*-type base of the same *p*-*i*-*n* SiNW shown in panel b at low magnification (left) and higher magnification (right), showing the amorphous nature of the deposited CoO_x; scale bars, 200 nm (left) and 10 nm (right).

4.3 Conclusions

We have developed a spatioselective photodeposition method that allows for deposition of co-catalyst materials on the MJ SiNW ends. The potential generated under illumination drives the reaction while the photocurrent drives selective reduction and oxidation at the n-type and p-type ends respectively. This method could be a powerful tool for creating functional

nanomaterials for other applications beyond PEC water-splitting, such as nanomotors[94]. To enable more precise control over the depositions, future work should focus on understanding the mechanism and relationship between variables in this process, such as light intensity, precursor concentration, and deposition time.

4.4 Acknowledgements

This work was performed in part at the Chapel Hill Analytical and Nanofabrication Laboratory, CHANL, a member of the North Carolina Research Triangle Nanotechnology Network, RTNN, which is supported by the National Science Foundation, Grant ECCS-2025064, as part of the National Nanotechnology Coordinated Infrastructure, NNCI. HRTEM and STEM-EDS measurements were performed in part by Dr. James McBride at the Vanderbilt Institute of Nanoscale Science and Engineering. Some photodepositions shown via SEM were performed by Michael Carter, an undergraduate researcher in the Cahoon lab.

.

CHAPTER 5: PHOTOELECTROCHEMISTRY OF MULTIJUNCTION SILICON NANOWIRES

5.1 Introduction

In order to test the viability of our MJ SiNW photocatalysts for PEC water splitting and compare them to other previously reported catalysts, it is necessary for us to measure their water-splitting performance in aqueous solutions. For a typical planar electrode, the water-splitting efficiency of a system is measured in a two or three-electrode cell where a potential may be applied (if necessary), photocurrent measured, and evolved product collected. While three-electrode cells are commonly used to determine half-cell efficiencies, two-electrode cells are more desirable because they can give the true device efficiency[95,96]. Two-electrode setups consist of a working electrode (i.e. the photoelectrode of interest) and a counter electrode immersed in a solution which are connected via an external circuit, usually a potentiostat. Under illumination, current may only flow if electrons and holes are reacting with solution species at the cathode and anode respectively, completing the circuit. The measured photocurrent can be used to calculate an STH efficiency if the Faradaic efficiency, the efficiency of reacted electrons that produce desired product, is known[95].

For PSRs, however, measuring photocurrent of the suspended particles in-situ is not feasible. Typically, the evolved gaseous products are measured via GC and this is used to calculate an STH. While STH is the best benchmark efficiency for comparing to other photocatalytic systems, diagnostic efficiencies such as external or internal quantum efficiencies

may be useful for understanding the material performance. The external quantum efficiency (EQE) is a function of wavelength and describes the number of incident photons that result in reacting electrons. The overall EQE is a product of each step of the water splitting reaction

$$EQE(\lambda) = \eta_{gen} \times \eta_{trans} \times \eta_{rxn} \quad (5.1)$$

where η_{gen}, η_{trans}, and η_{rxn} are the efficiency of electron-hole pair generation (i.e. absorption), charge transport, and reaction at the interface respectively. In a PSR, these contributing efficiencies are not easily disentangled, thus the commonly reported value is the apparent quantum yield (AQY)

$$\mathrm{AQY}(\lambda) = \frac{n_e * r_{H2}}{\Phi} \quad (5.2)$$

where n_e is the number of electrons participating in the reaction (2 for H_2 production), r_{H2} is the rate of gas production and Φ is the incident photon flux. AQY is a function of wavelength and is useful for understanding the overall STH and the limitations of the material.

Our SiNW photocatalysts are sufficiently large enough to fabricate single NW PEC devices in order to gain information about the single NW performance in addition to more traditional bulk PSR measurements. Here we describe the development of a single SiNW two-electrode setup and prototype PSR used to measure photoelectrochemical current and product generation, respectively, from our SiNW photocatalysts.

5.2 Results and Discussion

5.2.1 Single Nanowire Photoelectrochemistry

In order to test the photoelectrochemical viability of our functionalized SiNWs, we designed and constructed millimeter scale two-electrode devices to test single nanowire devices,

similar to those reported by Su et al[97]. Figure 5.1a shows a diagram and photo of the PDMS well that served as our vessel to contain solution. Metal contacts ran underneath the well to contact to one side of the wire and a macroscopic wire could be punctured through the sidewall as a counter electrode. The working and counter electrode were externally connected through a Keithley SourceAmmeter. In order to reduce the background current from the patterned metal contacts and the counter electrode, both of which have a much higher surface area than our working electrode, the metal contacts were coated in a layer of SiO_2 and SU-8 photoresist, and devices were illuminated using monochromatic light emitting diodes (LEDs). The SiNWs were also coated with SU-8, with the exception of the co-catalyzed tips, to minimize corrosion in solution. For all experiments shown here, the well was filled with pure deionized water.

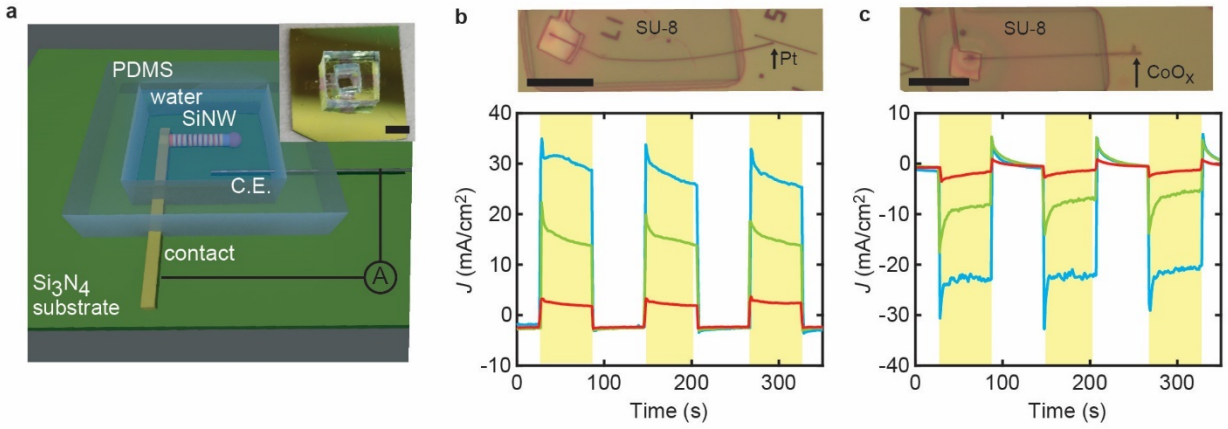

Figure 5.1: Single SiNW two-electrode measurements a, Schematic rendering of the single-SiNW two-electrode PEC cell. Inset: photograph of a cell; scale bar, 3 mm. **b-c**, Optical microscopy images (upper; scale bars, 20 μm) and chopped photocurrent vs. time (lower) for N = 40 co-functionalized SiNWs with the n-type/Pt photocathode end exposed (panel b) and the p-type/CoOx photoanode end exposed (panel c). Measurements were done at zero V_{app} under

illumination at 455 (cyan), 550 (green), and 650 nm (red) with intensities of 45, 56, and 29 mW/cm^2, respectively. Shaded areas indicate the time when the LED was on.

.

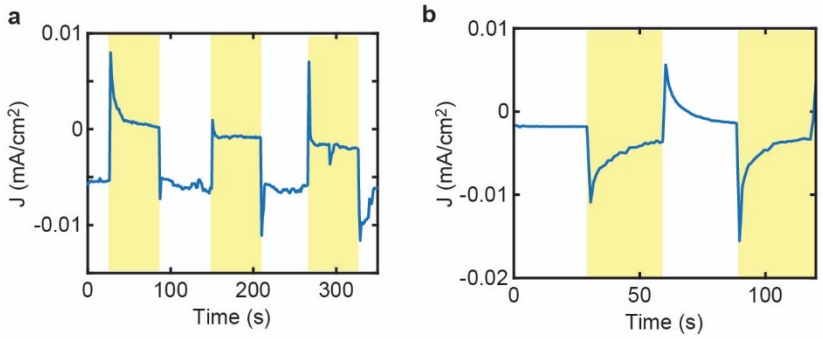

Figure 5.2: PEC control measurements. a-b, Photocurrent density for control electrodes (Pd/SiO_x/SU-8) identical to the electrodes used for electrical contact to the SiNWs measured against an Ir/IrO_x wire counter electrode (panel a) a Pt wire counter electrode (panel b) under chopped illumination (445 nm). Shaded areas indicate the time when the LED was on.

The scattering from the catalyst tip is just barely visible in bright field optical microscopy (Figure 5.1b-c), allowing us to correctly connect to the appropriate end of the wire. For counter electrodes, we used a Pt wire against the p-type/CoO_x working electrode and an Ir/IrO_x wire against the n-type/Pt working electrode. With zero externally applied bias and under chopped illumination with LEDs centered at 445, 549, and 650 nm, a clear photocathodic current (Figure 5.1b) and photoanodic current (Figure 5.1c) were observed for the SiNWs with the Pt and CoO_x ends exposed, respectively, which we attribute to the hydrogen and oxygen evolution reactions, respectively. While a photoresponse was observed for control electrodes (identical to those used to contact the wires), the magnitude was much lower and decayed quickly, suggesting a

primarily capacitive mechanism (Figure 5.2). Some attempts were made to measure the device performance under an applied bias, but this generally resulted in a large capacitive current that was hard to deconvolute from the Faradiac photocurrent

Table 5.1 Single Nanowire PEC Metrics

Working electrode	*D* (nm)	L_i (μm)	λ (nm)	LED power density (mW/cm^2)	I_{SC} *(pA)*	J_{SC} [a] (mA/cm^2)	EQE[a]
$(p\text{-}i\text{-}n)_{40}$-/Pt	286	1.0	445	45	75	26 (16)	1.6 (1.0)
			549	56	40	14 (8.7)	0.56 (0.35)
			650	29	5.4	1.9 (1.1)	0.12 (0.08)
$(n\text{-}i\text{-}p)_{40}$-/CoOx	213	1.0	445	45	45	21 (13)	1.3 (0.82)
			549	56	15	7.0 (4.4)	0.28 (0.18)
			650	29	4	1.9 (1.2)	0.12 (0.08)

[a] Assuming cross sectional area equal to projected area of one intrinsic segment. Parenthetical value is assuming cross sectional area equal to projected area of one *p-i-n* segment.

Calculated and measured PEC metrics are shown in Table 5.1. Since we expect IQE to be nearly zero in the n and p-type segments, we calculated a J_{SC} from the projected area of one intrinsic segment. J_{SC} decreases as wavelength increases, as expected from the wavelength-dependent absorption of Si and the lower power density of the LED at 650 nm. The photocurrent from the photoanodic SiNW is slightly less than the photocathodic SiNW, which suggests that the water oxidation reaction proceeds with less efficiency. This lower efficiency is consistent with the poor efficiency of CoO_x as an OEC under pH 7 conditions[98], although the large overpotential provided by the $N = 40$ SiNWs is likely to mitigate the otherwise low efficiency. The J_{SC} measured here are also substantially higher than those seen in our single NW PV devices

(Figure 3.3g). This can be explained by an increased absorption of the short-wavelength LED lighting and surface passivation effects of the SU-8, as demonstrated in Figure 5.3.

When calculating for absorption in the intrinsic section only, the calculated EQE for both electrodes under 445 nm illumination is greater than unity. EQEs greater than 1 in NWs are not unprecedented in the literature, since the nanowire antennae effect can result in an absorption cross section greater than physical cross section[99,100]. However, the large improvements we see in the I_{SC} for SU-8-coated PV devices suggest we could be collecting substantial photocurrent from the *n/p* type segments. By including them in our projected area, we get more reasonable J_{SC} and EQE values, shown in the parentheses in Table 5.1. Finally, we note that there is some uncertainty with the exact photon flux to the NW surface, since the LED power density was averaged over a much larger area than the area of the NW itself.

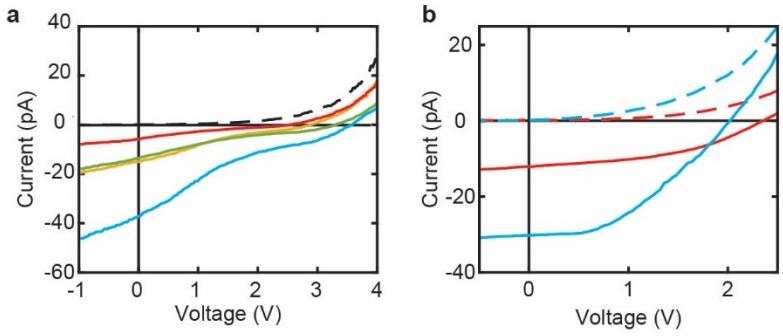

Figure 5.3: Effect of LED illumination and SU-8 coatings on SiNW PVs. a, *I-V* curves of an N=15 SiNW PV device in the dark (dashed), under 1-sun illumination (yellow), and under LED illumination of wavelengths 445 nm (cyan), 549 nm (green), and 650 nm (red). **b,** *I-V* curve of a *N*=10 SiNW PV device in the dark (dashed lines) under 1-sun illumination (solid lines) with no coating (red) and after coating with a layer of SU-8 (cyan).

5.2.1 Optical Properties of SiNWs Suspensions

Unlike all single SiNW measurements presented thus far, where all junctions are illuminated uniformly from a normal incident angle, in a PSR the MJ SiNWs are free to rotate and the angle of illumination is variable, resulting in variable illumination of axial junctions, potentially introducing problems with photocurrent matching. In bulk planar Si solar cells, the number of junctions is typically limited to three due to optical losses from competitive absorption in the upper junctions and reflections at junction interfaces[101]. Nanowires, however, have geometry-dictated optical resonances that can be used to engineer desirable absorption properties[99,102].

To determine the angle-dependent photocurrent of a SiNW, we built a finite-element model in COMSOL Multiphysics that included a 32 μm long SiNW broken into ten junctions of realistic experimental length (Figure 5.4a) being illuminated by planewave light at various angles of incidence (θ). Simulations were run under TE and TM polarizations for each angle and the average was taken to determine the absorption spectrum of an unpolarized illumination. The peaks in absorbed power result from nanophotonic resonances in the wire, resulting in an absorption spectrum that looks quite different than bulk Si (Figure 5.4b). Absorption profiles at 550 nm illumination in Figure 5.4c show essentially uniform absorption across the wire at nearly all angles of illumination with some increased absorption at the tips due to end scattering effects. Interestingly, under coaxial illumination there is actually more absorption at 550 nm in the furthest junction of the wire than in the nearest junction, which is due to a shift in the peak absorption with junction index, j (Figure 5.4b inset). J_{SC} for each junction was calculated at various angles of illumination by integrating the photon absorption spectra within each segment, assuming the AM1.5G solar spectrum and an IQE of unity. The resulting photocurrent in each

junction is nearly uniform, shown in Figure 5.4d, which is in stark contrast to a bulk Si solar cell of identical thickness. End scattering effects tend to increase absorption in the first and last junction by ~10%, but the intermediate junctions show the same J_{SC} within ~15%, even for illumination coaxial with the SiNW. To determine a weighted average absorption, we calculated the probability of a wire being illuminated at each value of θ by accounting for identical results when rotating in a third dimension (ϕ) at each angle and assuming an isotropic distribution (Figure 5.4e). This results in a weighted average photocurrent (dashed line, Figure 5.4d) similar to the 30° illumination result.

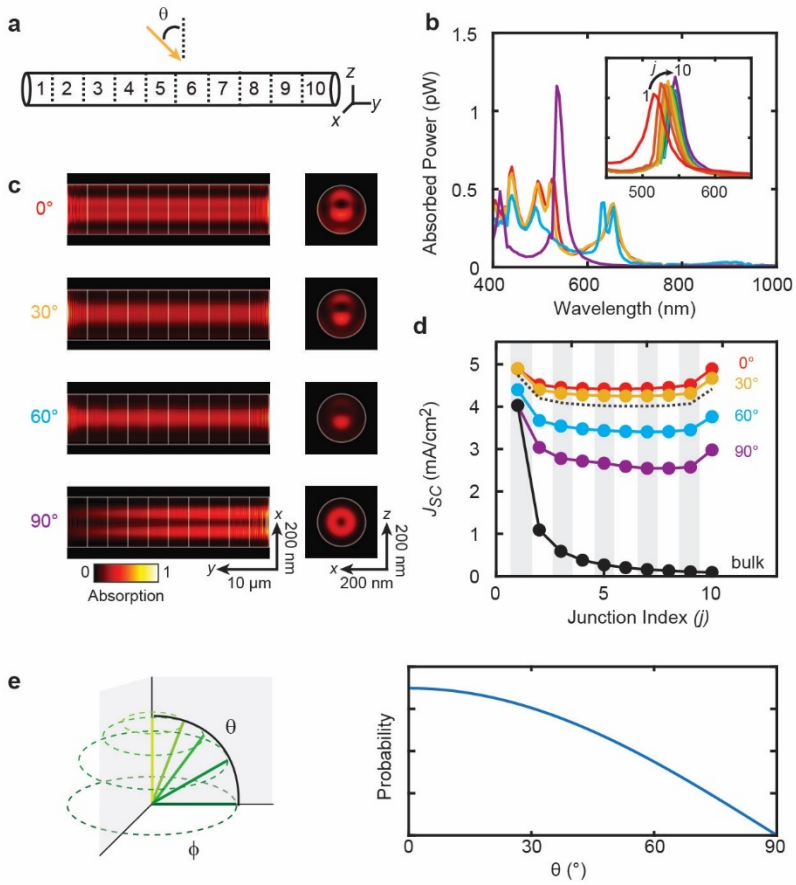

Figure 5.4: Simulated absorption and calculated photocurrent from a SiNW. a, Simulated geometry of a 32 μm long SiNW divided into 10 junctions, labeled by junction index *j*, where the illumination angle, θ, is defined versus the surface normal. **b,** Absorbed power spectrum for $j = 5$ under AM1.5G solar illumination at an incident angle of 0 (red), 30 (yellow), 60 (cyan), and 90° (violet). Inset shows the shift in absorption peak at 90° illumination with increasing *j*. **c**, Normalized axial (left) and radial (right) absorption profiles at 550 nm at incident angles of 0, 30, 60, and 90°. d, J_{SC} for each junction at various angles of illumination. Black dots show photocurrent of a bulk $N = 10$ solar panel with the same junction thickness. The grey dashed line shows the weighted average expected J_{SC} assuming a three-dimensional isotropic distribution of SiNWs. **e,** Schematic of all possible 3D rotation angles and the probability distribution of each possible value of θ used to calculate the weighted average photocurrent in panel d.

The optical properties of SiNW PSRs were tested experimentally by suspending functionalized MJ SiNWs into aqueous pH 3 sulfuric acid solution. PSRs with $N = 5$, 15, and 40 at concentrations of ~2000, ~1000, and ~600 SiNWs/μL, respectively, were prepared and exhibited a cloudy appearance with extinction spectra showing several peaks and effective extinction coefficients above ~1 cm^{-1} (Figure 5.5a). Interestingly, the simulated extinction spectrum, calculated by adding the weighted average absorption and weighted average scattering of a single NW (Figure 5.5a, dashed line) reproduces the general features of the PSR extinction spectra. Comparison to the simulated scattering spectrum (Figure 5.5a, gray dotted line) indicates that the PSR optical properties are dominated by the scattering rather than absorption characteristics of the SiNWs, as has also been observed for disordered SiNW fabric[103]. By using an integrating sphere, we can collect both the transmitted and scattered light and get a true absorbance spectrum, shown in Figure 5.5b. The general shape of the absorption spectrum follows the bulk Si absorption coefficient, although upon closer inspection, there are some features. By fitting the spectrum to an exponential decay and plotting the residuals (Figure 5.5c), we reveal peaks that closely match the COMSOL-simulated absorption of a single SiNW.

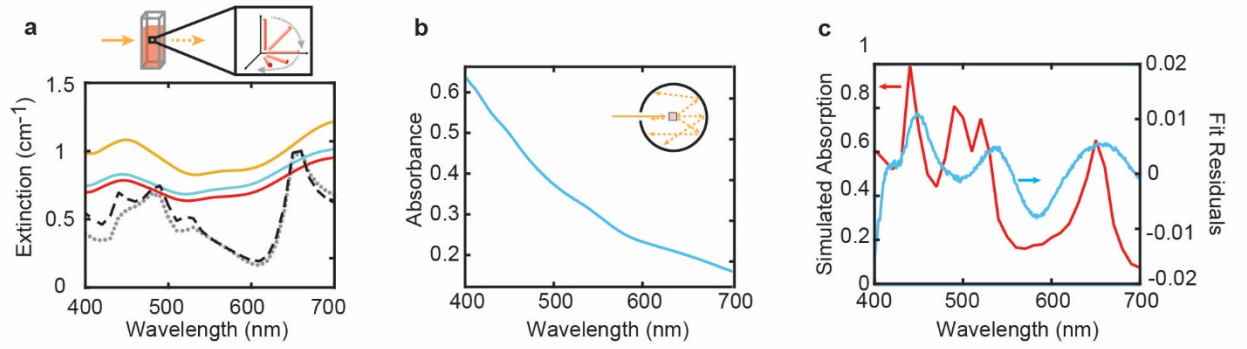

Figure 5.5: Optical Properties of SiNW suspensions. a, Upper: Schematic illustration of extinction measurements on an isotropic distribution of SiNWs in a standard cuvette. Lower: extinction spectra (solid lines) of suspensions of SiNWs with $N = 5$ (yellow), 15 (red), and 40 (cyan). The dashed and dotted lines are extinction and scattering spectra, respectively, from optical simulations. **b**, Absorbance spectrum of a SiNW suspension using an integrating sphere. Inset: Schematic of measurement collection inside the sphere. **c,** Residuals of an exponential fit to the spectrum in panel b (blue) and the weighted average absorption spectrum calculated for a single 200 nm diameter SiNW in COMSOL.

5.2.3 Product Evolution from SiNW PSRs

For measurement of hydrogen generation, suspensions were loaded into an ~12 mL cell (Figure 5.6a), purged with argon gas, illuminated with LEDs of variable wavelengths, and periodically sampled for analysis by GC. H_2 production metrics are shown in Table 5.2. Note that SiNWs used in the PSRs were not hydrogen annealed because the high-temperature processing was not compatible with the co-catalyst deposition steps. For $N = 40$ SiNWs under 650 nm LED illumination, we observed clear hydrogen production over several hours with a steady increase in hydrogen with time (Figure 5.6b). Moreover, the hydrogen production rate increased approximately linearly with illumination intensity (Figure 5.6c). Note that no hydrogen

was detected from control PSRs composed of MJ SiNWs without HEC and OEC catalysts. Suspensions were found to produce hydrogen for several days, after which performance decreased. Based on SEM images, the only apparent degradation of the SiNWs was dissolution of CoO_x catalyst, which is expected under pH 3 conditions[98]. The relatively good stability of the SiNWs may be a result of the degenerate n- and p-type doping levels, which act as an etch stop in aqueous solution[58], and the strong electric field in the intrinsic segments[51]. The CoO_x catalyst is more stable in pure water and we observed an increase in hydrogen concentration over several days when using pH 7 water (Figure 5.7a), but the generation rate was lower than in the acidic solution. Note that hydrogen production with 650 nm illumination is the longest wavelength ever to be reported for a PSR.

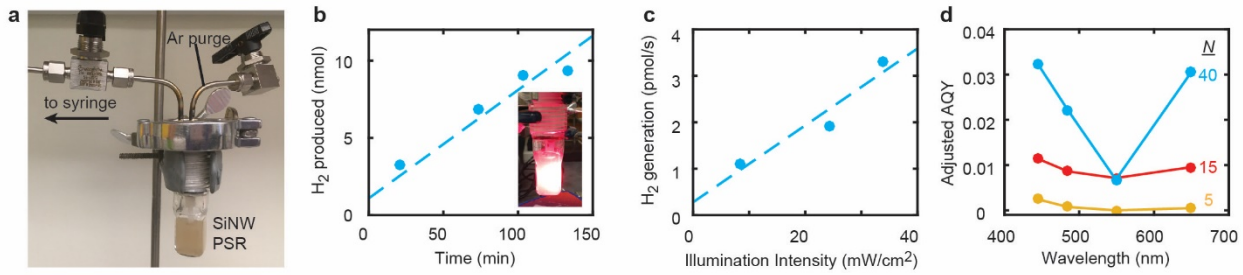

Figure 5.6: Product evolution from MJ SiNW Particle Suspension Reactors. a, Photograph of the ~12 mL liquid cell used to evaluate SiNW-based PSRs. **b**, Total hydrogen generated as a function of time for a N = 40 PSR with 650 nm LED illumination at 34 mW/cm2. **c**, Hydrogen generation rate as a function of light intensity from a N = 40 PSR with 650 nm LED illumination. **d**, Adjusted AQY for hydrogen generation as a function of LED illumination wavelength for N = 5 (yellow), 15 (red), and 40 (cyan) PSRs.

Table 5.2: PEC metrics for MJ SiNW PSRs

N	PSR OD @450 nm	L_i (μm)	LED wavelength (nm)	LED power density (mW/cm^2)	H_2 generation rate (nmol/hr)	AQY[a] (%)
5	3.7	1.5	445 ± 34	44	13.7	0.0026
			485 ± 20	36	3.64	0.0008
			549 ± 15	56	B.D.L[a]	-
			650 ± 13	33	3.01	0.0005
15	2.7	1.5	445 ± 34	44	17.4	0.0033
			485 ± 20	36	11.5	0.0025
			549 ± 15	56	17.2	0.0021
			650 ± 13	33	16.1	0.0028
40	2.9	1	445 ± 34	48	14.6	0.0025
			485 ± 20	40	9.13	0.0017
			549 ± 15	59	4.63	0.0005
			650 ± 13	34	14.1	0.0024

[a] B.D.L. = below detection limit

PSRs with $N = 5$, 15, and 40 were illuminated at four LED wavelengths, and the apparent quantum yield (AQY) for hydrogen generation was measured at each wavelength, with all metrics collected in Table 5.2. To enable direct comparisons on the basis of photons absorbed per *p-i-n* junction between PSRs with different *N* and SiNW concentrations, an adjusted AQY (Figure 5.6d) was calculated by multiplying the AQY (%) by *N* and dividing by the product of L_i (μm) and optical density (OD). All suspensions produced hydrogen, and the AQY values tended to peak for illumination at 445 nm and 650 nm and dip at 485 and 550 nm, which was in approximate agreement with the extinction spectra of the samples (Figure 5.4a). This agreement suggests that the overall sample absorption and hydrogen generation is correlated with the scattering response of the SiNWs, which will increase the effective optical path length through the cell. The $N = 5$ PSRs produced the lowest adjusted AQY likely because a large fraction of the

SiNWs did not generate the photovoltage needed for water splitting, and the $N = 40$ PSR was 10-20 times more efficient on a photon absorbed per junction basis at generating hydrogen than the $N = 5$ PSR. Thus, there is substantial opportunity in future MJ SiNW PSR designs to optimize N, SiNW lengths, *p-i-n* junction geometry and performance, diameter, and SiNW concentration to optimize light absorption and AQY. Additionally, in the presence of citric acid (a sacrificial electron donor), the AQY from an $N = 40$ PSR increased substantially (Figure 5.7b) suggesting that the OER reaction is limiting the reaction rate and that further engineering of the OER co-catalyst and solution environment may be necessary for efficient fuel generation.

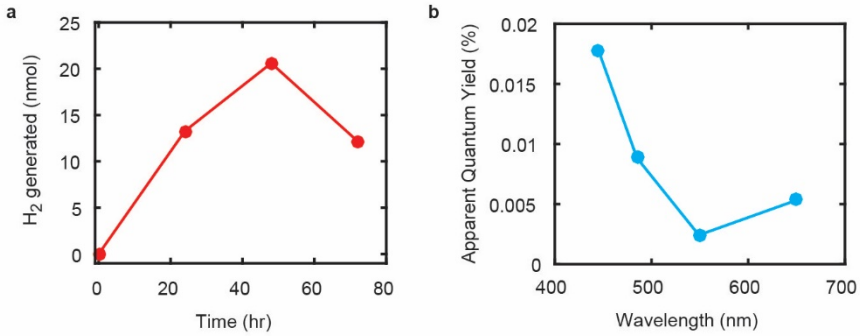

Figure 5.7: Hydrogen generation in PSRs in pH 7 water and pH 3 citric acid solution. a, Total hydrogen gas produced by an $N = 15$ PSR over the course of several days in deionized water (pH 7) under 650 nm illumination. Values are corrected for hydrogen removed during sampling process. The apparent decrease in H_2 generation after two days is likely due to a stop in H_2 generation combined with leakage from the cell. **b**, Quantum yield of an $N = 40$ PSR in an aqueous citric acid solution (pH 3) under various wavelengths of LED illumination.

5.4 Conclusions

We have used both single SiNW photoelectrochemical measurements as well as prototype PSRs to characterize the solar water splitting ability of the SiNW particulate photocatalysts. The two-electrode measurements show that functionalized wires can produce high photoelectrochemical current under zero-applied bias, indicating that water splitting is occurring. This photocurrent is likely enhanced by the passivation of the SU-8 polymer coating, limiting our ability to relate it directly to PSR performance. Nonetheless, this single nanowire measurement could be used in the future to vet different co-catalysts to optimize material choice, deposition thickness, etc. Our PSR experiments demonstrated the ability of these catalysts to do unassisted water-splitting to produce measurable H_2 gas. Interestingly, the AQY of the reactors related closely to their experimental extinction spectra and simulated single NW spectra, highlighting the ability to use photonic engineering of the wires to produce desirable optical effects such as spectrum splitting, light-trapping resonances, etc. While the efficiency of our PSRs are still quite low, future efforts to lower surface recombination, optimize co-catalysts, and increase the number of viable wires in suspension should result in an increase in performance.

CONCLUSIONS AND FUTURE DIRECTIONS

Solar water splitting and other forms of PEC fuels production are a promising route to clean energy. PSRs offer the best chance at synthesizing these fuels at a cost per kg that is competitive with the current price of fossil fuels, allowing an economically feasible transition towards a net zero carbon fuel cycle. To realize these systems, we still need a broadband absorbing and earth abundant particulate photocatalyst that is capable of reasonable STH efficiencies. As seen in this work, the bottom-up VLS growth of SiNWs enables the synthesis of MJ nanophotovoltaic devices with photovoltages that increase linearly with number of junctions. This allows for the design of MJ SiNW PVs that produce a specific voltage for the desired function, opening up their application space. Here we have explored one possible application, solar water splitting, and have used the asymmetric geometry and potential gradient to spatioselectively deposit co-catalyst materials. The electrons and holes generated in the structure can reduce and oxidize, respectively, metal ions in solution to result in a Janus-like nanoreactor. We have measured appreciable photoelectrochemical current from functionalized single SiNWs and small amounts of H_2 produced from wires suspended in aqueous solutions. This is the first report of a SiNW MJ nanoparticle greater than two junctions and the first time a Si nanoparticle has been used in a PSR type water-splitting reactor.

While we believe these results have been promising, this initial demonstration of a SiNW PSR has a rather low AQY and therefore low theoretical STH efficiency. Future work must be done to understand the cause of these inefficiencies and improve performance to make these

particles viable for commercial use. To break down the ways that these systems may be better understood and improved, we can look again to the three processes involved in solar water splitting: light absorption, charge separation/transport, and reaction.

At the single NW level, the absorption from the wires could be improved by tuning the geometry of the wires using the ENGRAVE method (Encoded Nanowire Growth and Appearance through VLS and Etching). SiNW gratings exhibit resonances in the visible and IR that have high quality factors and could enable high absorbances at specific wavelengths in the MJ stuctures[104,105]. Additionally, by increasing the ratio of intrinsic Si to doped Si in the MJ superlattices, we can increase absorption and thus photocurrent of these wires.

To achieve more efficient charge separation, the most pressing problem is that of surface recombination, especially at defects at the Si/SiO_x interface, which is extremely detrimental to axial SiNW PVs. Since the typical high-temperature annealing procedures are incompatible with our co-catalyst depositions, a lower temperature passivation of the Si/SiO_x interface is greatly needed. In previous literature a low temperature anneal with radical hydrogen atoms has been reported to improve the performance of Si electronics[106] and a similar process could be implemented with our wires. We have recently constructed a hot-wire tungsten filament reactor that can be connected to the CVD system, though robust testing of SiNW PVs is still needed to confirm its efficacy.

Finally, the selection and deposition of co-catalyst materials can be tested and optimized to achieve a high catalytic activity while keeping light blocking, defect introduction, and side-reactions low. Single NW PEC devices could be useful in the future for vetting this deposition and determining the best choice of material and optimal thickness. While Pt and CoO_x are some of the most efficient catalysts for the HER and OER reactions, more sophisticated catalysts

would be desirable for our MJ SiNWs to increase stability and decrease competing reactions. Preliminary evidence suggests that we can deposit rhodium/chromium oxide (Rh/Cr_2O_3) core/shell structures onto our SiNWs (Figure 6.1a,c), which have been used in literature to prevent oxygen from reaching the noble metal catalyst. The photodeposition of Cr_2O_3 from a K_2CrO_7 solution occurs through a reduction mechanism and, interestingly, we only see formation of the Cr_2O_3 shell if the reaction cell is purged with argon beforehand, suggesting that the Cr ion reduction is competing with the oxygen reduction reaction. Additionally, we are able to photodeposit Co-Pi (Figure 6.1b,d), a cobalt phosphate catalyst that is "self-healing" and operates very well at neutral pHs[107,108] which could replace our less stable CoO_x. Figure 6.1 shows initial characterization of these structures.

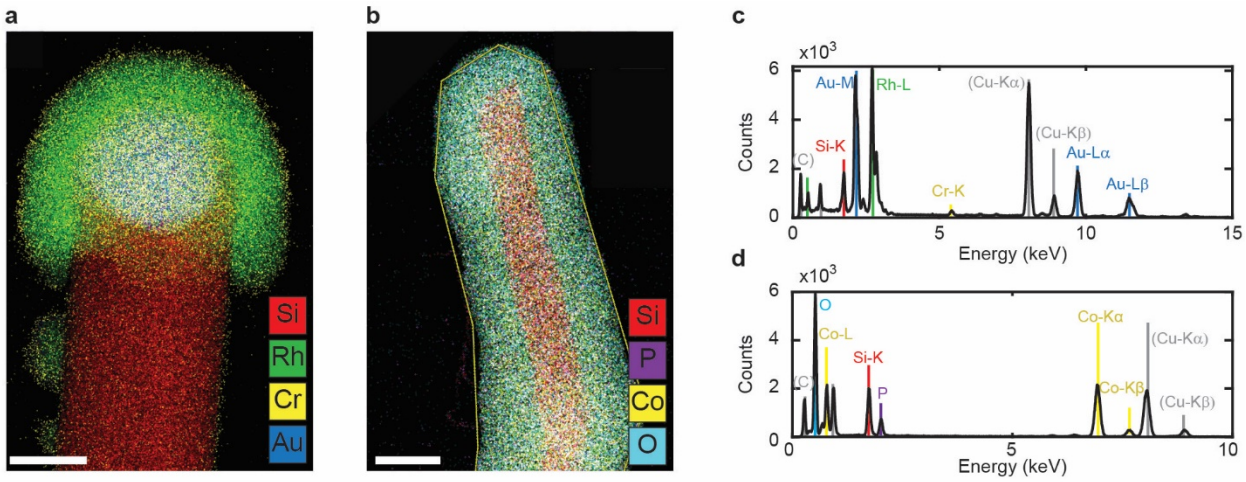

Figure 6.1 STEM EDS of alternative co-catalyst materials. a, STEM-EDS map Rh-CrOx core-shell photodeposition. Scale bar, 100 nm. **b,** STEM-EDS map of Co-Pi photodeposition. Scale bar, 300 nm. **c,** EDS energy spectrum for Rh-CrOx shown in panel a. **d,** EDS energy spectrum for Co-Pi shown in panel b.

In regards to optimization of the suspensions, there are many ways that these suspensions could be engineered to produce more H_2. One exciting opportunity to improve light absorption in the suspension would be to use photon management and spectrum splitting by incorporating many different wire geometries in the same suspension that scatter and absorb at complementary wavelengths (Figure 6.2). A Monte Carlo-based photon diffusion model[109,110] would likely be needed to more accurately describe the multiple scattering events in the suspensions and help design such a mixture. Another way to maximize suspension efficiency would be to reduce the percentage of broken, unfunctionalized, or otherwise defective Si particles that contribute to competitive absorption and product recombination. This could be done by further optimizing growth conditions to improve the yield of long, straight wires on the growth substrate, finding a gentler method of NW removal from the substrate, or developing a strategy for separating out viable SiNWs from non-viable pieces. To improve the reactivity of the co-catalysts, the aqueous solution could be altered to have a different pH or electrolyte concentration. For example, switching to a potassium phosphate (KPi) buffer could enhance the OER reaction by improving stability and efficiency of a CoPi OER co-catalyst.

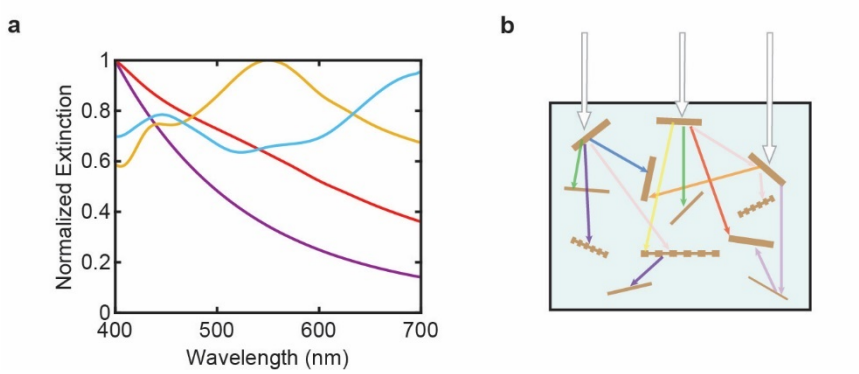

Figure 6.2 Geometry dependent optical properties. a, Experimentally measured extinction spectra (normalized) of SiNW suspensions of different diameters: 20 nm (violet), 50 nm (red), 100 nm (yellow), and 200 nm (blue). **b,** Schematic representation of a proposed spectrum-splitting PSR where SiNWs scatter and absorb at complementary wavelengths to each other.

Beyond PSR water splitting, the ability to synthesize SiNWs with large tunable photovoltages could have implications in a variety of other applications. We expect that similar particulate photocatalyst structures could be designed, synthesized, and functionalized for other PEC reactions such as CO_2 reduction or nitrogen fixation. Miniature MJ SiNWs functionalized with the appropriate materials could be used as electrophoresis-driven[94] or magnetically-driven nanomotors.[111]

APPENDIX

Theoretical model for multijunction *I-V* behavior

This brief script written in MATLAB generates an *I-V* curve for single junctions from an input of performance metrics (at beginning of script) and then calculates the resulting *I-V* curve for a MJ device consisting of those diodes in series. The model assumes ideal behavior with affects from shunt resistance and a series resistance that is limited by the tunnel junction resistance. This model is only valid in the forward bias regime where $V_{app} < V_{OC}$ and does not account for other diode phenomena such as junction breakdown. Required inputs are N and the device metrics for each junction (I_{SC}, Io, n, R_{sh}). The script outputs three data structures (*I-V* data for single junctions, *I-V* data for MJ, and *I-V* data for MJ with tunnel junctions) and two plots (single junction *I-V* curves and MJ *I-V* curves with and without effect of tunnel junctions).

```
%Single junction metrics
N = 3; %number of junctions
Ntj = N-1; %number of tunnel junctions
Io=[5E-14,5E-14,5E-14]; %dark sat current in amps
n=[2,2,2]; %ideality factor
Isc=[2.5E-11,2.7E-11,3E-11]; %short circuit current in amps
Rsh=[5E11,5E11,5E11]; %shunt resistance in ohms
Vrange=[-0.5,0.5]; %voltage range for applied voltage in volts
numpts= 50000; %number of points taken on IV curve (higher = more accurate
but longer calc)
Rtj=8.72e8; %tunnel junction resistance in ohms

%generating I-V curves for single junctions
IV=struct();
count=1;
V=linspace(Vrange(1),Vrange(2),numpts);
for i=1:length(Isc)
    for j=1:length(V)
        I(j)=-Io(i)*(exp(38.95*V(j)/n(i))-1)+Isc(i)-V(j)/Rsh(i);
    end
    IV(count).voltage=V;
    IV(count).current=I;
    IV(count).Isc=Isc(i);
    IV(count).Io=Io(i);
    IV(count).ideality=n(i);
    IV(count).shunt=Rsh(i);
    count=count+1;
end
```

```
%plotting all single junctions on the same graph
figure;hold on
for i=1:length(IV)
    plot(IV(i).voltage,IV(i).current.*-1e12);
end
axis([-0.1,0.4,max([Isc]).*-1.1e12,5]);
xlabel('Voltage(V)')
ylabel('Current(pA)')
box on;
clear i

%Finding the voltages where the currents are equal in all diodes
Iref=linspace(0,35e-12,numpts);
multiIV=struct();
count=1;
for i=1:length(IV);
    for k=1:length(Iref);
        [u,v]=min(abs(Iref(k)-IV(i).current));
        V(k)=IV(i).voltage(v);
    end
    multiIV(count).voltage=V;
    multiIV(count).refcurrent=Iref;
    count=count+1;
end
clear u v i k Isc Rsh n Io n Vrange

% Adding together the voltages of the multijunction where their currents
% are equal
Vmj=0;
for j=1:length(multiIV);
    Vmj=Vmj+multiIV(j).voltage;
end
MJ_IV=struct();
MJ_IV.V=Vmj;
MJ_IV.I=Iref;
[a,b]=min(abs(Vmj-0));%yintercept
[c,d]=min(abs(Iref-0));%xintercept
Xintcurrent=Iref(d:d+10);
Xintvoltage=Vmj(d:d+10);
Yintcurrent=Iref(b-10:b+10);
Yintvoltage=Vmj(b-10:b+10);
z=polyfit(Xintcurrent,Xintvoltage,1); %linear fit of x-int data to get Voc
and Rs
MJ_IV.Voc=z(1,2); %opencircuitvoltage
i=polyfit(Yintvoltage,Yintcurrent,1); %linera fit of y-int data to get Isc
and Rsh
MJ_IV.Isc=abs(i(1,2));%short circuit current
MJ_IV.Rsh=1./abs(i(1,1));%shunt resistance
MJ_IV.Rs=abs(z(1,1));%series resistance
MJ_IV.power=Vmj.*Iref;%power
MJ_IV.maxpower=max(MJ_IV.power);%maxpower
MJ_IV.FF=MJ_IV.maxpower./(MJ_IV.Voc.*MJ_IV.Isc);%fill factor

%plotting MJ IV curve
figure;
```

```
plot(MJ_IV.V,MJ_IV.I.*-1e12)
hold on;box on
axis([-0.1,MJ_IV.Voc*1.1,MJ_IV.Isc.*-1.1e12,5]);
xlabel('Voltage(V)')
ylabel('Current(pA)')

% clear unimportant variables
clear i j k u v count a b c d Xintcurrent Xintvoltage Yintcurrent Yintvoltage
z multiIV numpts

%Tunnel junctions

for i=1:length(Iref)
    Vf(i)=Vmj(i)-(Iref(i)*Rtj*Ntj);%subtracting voltage drop across the
tunnel junctions
end

%calculating diode metrics and compiling into structure
MJ_TJ_IV=struct();
MJ_TJ_IV.voltage=Vf;
MJ_TJ_IV.current=Iref;
[a,b]=min(abs(Vf-0));%yintercept
[c,d]=min(abs(Iref-0));%xintercept
Xintcurrent=Iref(d:d+10);
Xintvoltage=Vf(d:d+10);
Yintcurrent=Iref(b-10:b+10);
Yintvoltage=Vf(b-10:b+10);
z=polyfit(Xintcurrent,Xintvoltage,1); %linear fit of x-int data to get Voc
and Rs
MJ_TJ_IV.Voc=z(1,2); %opencircuitvoltage
i=polyfit(Yintvoltage,Yintcurrent,1); %linear fit of y-int data to get Isc
and Rsh
MJ_TJ_IV.Isc=abs(i(1,2));%short circuit current
MJ_TJ_IV.Rsh=1./abs(i(1,1));%shunt resistance
MJ_TJ_IV.Rs=abs(z(1,1));%series resistance
MJ_TJ_IV.power=Vf.*Iref;%power
MJ_TJ_IV.maxpower=max(MJ_TJ_IV.power);%maxpower
MJ_TJ_IV.FF=MJ_TJ_IV.maxpower./(MJ_TJ_IV.Voc.*MJ_TJ_IV.Isc);%fill factor

%plotting IV curve
plot(Vf,Iref.*-1e12)
axis([-0.1,MJ_TJ_IV.Voc*1.1,MJ_TJ_IV.Isc.*-1.1e12,5]);
xlabel('Voltage(V)')
ylabel('Current(pA)')
legend('no TJs','TJs')

% clear rest of variables
clear i j k u v count N Ntj V Vmj I Iref Rtj a b c d Xintvoltage Xintcurrent
Yintcurrent Yintvoltage z Vf
```

REFERENCES

1 *Global direct primary energy consumption*, <https://ourworldindata.org/grapher/global-primary-energy?time=earliest..1986> (2019).

2 Pierce, E. R. *Top 6 Things You Didn't Know About Solar Energy*, <https://www.energy.gov/articles/top-6-things-you-didnt-know-about-solar-energy> (2016).

3 Copeland, A. W., Black, O. D. & Garrett, A. B. The Photovoltaic Effect. *Chem. Rev.* **31**, 177-226 (1942).

4 Fritts, C. E. On a new form of selenium cell, and some electrical discoveries made by its use. *Am. J. Sci.* **s3-26**, 465 (1883).

5 Ohl, R. S. Light-sensitive electric device. U.S. patent 2443542A (1946).

6 Chapin, D. M., Fuller, C. S. & Pearson, G. L. A New Silicon p-n Junction Photocell for Converting Solar Radiation into Electrical Power. *J. Appl. Phys.* **25**, 676-677 (1954).

7 Ritchie, H. & Roser, M. *Renewable Energy*, <https://ourworldindata.org/renewable-energy> (2017).

8 Fujishima, A. & Honda, K. Electrochemical photolysis of water at a semiconductor electrode. *Nature.* **238**, 37-38 (1972).

9 McKone, J. R., Lewis, N. S. & Gray, H. B. Will Solar-Driven Water-Splitting Devices See the Light of Day? *Chem. Mater.* **26**, 407-414 (2014).

10 Pinaud, B. A. et al. Technical and economic feasibility of centralized facilities for solar hydrogen production via photocatalysis and photoelectrochemistry. *Energy Environ. Sci.* **6**, 1983-2002 (2013).

11 Fabian, D. M. et al. Particle suspension reactors and materials for solar-driven water splitting. *Energy Environ. Sci.* **8**, 2825-2850 (2015).

12 Wang, Q. & Domen, K. Particulate photocatalysts for light-driven water splitting: mechanisms, challenges, and design strategies. *Chem. Rev.* **120**, 919-985 (2020).

13 Iwashina, K., Iwase, A. & Kudo, A. Sensitization of wide band gap photocatalysts to visible light by molten CuCl treatment. *Chem. Sci.* **6**, 687-692 (2015).

14 Porob, D. G. & Maggard, P. A. A Rapid Flux-Assisted Synthetic Approach Towards the Bandgap Engineering of Layered Perovskites. *Chem. Mater.* **19**, 970-972 (2007).

15 Willkomm, J. et al. Dye-sensitised semiconductors modified with molecular catalysts for light-driven H_2 production. *Chem. Soc. Rev.* **45**, 9-23 (2016).

16 Umebayashi, T., Yamaki, T., Itoh, H. & Asai, K. Analysis of electronic structures of 3d transition metal-doped TiO_2 based on band calculations. *J. Phys. Chem. Solids* **63**, 1909-1920 (2002).

17 Wang, J., Su, S., Liu, B., Cao, M. & Hu, C. One-pot, low-temperature synthesis of self-doped $NaTaO_3$ nanoclusters for visible-light-driven photocatalysis. *Chem. Commun.* **49**, 7830-7832 (2013).

18 Qian, K. et al. Surface Plasmon-Driven Water Reduction: Gold Nanoparticle Size Matters. *J. Am. Chem. Soc.* **136**, 9842-9845 (2014).

19 Zhao, J., Holmes, M. A. & Osterloh, F. E. Quantum Confinement Controls Photocatalysis: A Free Energy Analysis for Photocatalytic Proton Reduction at CdSe Nanocrystals. *ACS Nano* **7**, 4316-4325 (2013).

20 Luo, L. & Maggard, P. A. Effect of ligand coordination on the structures and visible-light photocatalytic activity of manganese vanadate hybrids. *Cryst. Growth Des.* **13**, 5282-5288 (2013).

21 Wang, D. et al. Core/Shell Photocatalyst with Spatially Separated Co-Catalysts for Efficient Reduction and Oxidation of Water. *Angew. Chem. Int. Ed.* **52**, 11252-11256 (2013).

22 Gao, Y. et al. Directly Probing Charge Separation at Interface of TiO_2 Phase Junction. *J. Phys. Chem. Lett.* **8**, 1419-1423 (2017).

23 Jang, J. S., Kim, H. G. & Lee, J. S. Heterojunction semiconductors: A strategy to develop efficient photocatalytic materials for visible light water splitting. *Catal. Today* **185**, 270-277 (2012).

24 Chen, R., Zhu, J., An, H., Fan, F. & Li, C. Unravelling charge separation via surface built-in electric fields within single particulate photocatalysts. *Faraday Discuss.* **198**, 473-479 (2017).

25 Seh, Z. W. et al. Combining theory and experiment in electrocatalysis: Insights into materials design. *Science.* **355**, eaad4998 (2017).

26 Dalle, K. E. et al. Electro- and Solar-Driven Fuel Synthesis with First Row Transition Metal Complexes. *Chem. Rev.* **119**, 2752-2875 (2019).

27 Tabata, S., Nishida, H., Masaki, Y. & Tabata, K. Stoichiometric photocatalytic decomposition of pure water in Pt/TiO_2 aqueous suspension system. *Catal. Lett.* **34**, 245-249 (1995).

28 Liu, H. et al. Roles of Bi, M and VO_4 tetrahedron in photocatalytic properties of novel $Bi_{0.5}M_{0.5}VO_4$ (M=La, Eu, Sm and Y) solid solutions for overall water splitting. *J. Solid State Chem.* **186**, 70-75 (2012).

29 Maeda, K. et al. Photocatalyst releasing hydrogen from water. *Nature.* **440**, 295-295 (2006).

30 Maeda, K. & Domen, K. Photocatalytic water splitting: recent progress and future challenges. *J. Phys. Chem. Lett.* **1**, 2655-2661 (2010).

31 Fountaine, K. T., Lewerenz, H. J. & Atwater, H. A. Efficiency limits for photoelectrochemical water-splitting. *Nat. Commun.* **7**, 13706 (2016).

32 Beiser, V. *The World in a Grain*. (Riverhead Books, New York, 2018).

33 Gao, X. et al. Structured silicon for revealing transient and integrated signal transductions in microbial systems. *Science Advances* **6**, eaay2760 (2020).

34 Parameswaran, R. et al. Photoelectrochemical modulation of neuronal activity with free-standing coaxial silicon nanowires. *Nat. Nanotechnol.* **13**, 260-266 (2018).

35 Tian, B., Kempa, T. J. & Lieber, C. M. Single nanowire photovoltaics. *Chem. Soc. Rev.* **38**, 16-24 (2009).

36 Garnett, E. & Yang, P. Light Trapping in Silicon Nanowire Solar Cells. *Nano Lett.* **10**, 1082-1087 (2010).

37 Tsakalakos, L. et al. Silicon nanowire solar cells. *Appl. Phys. Lett.* **91**, 233117 (2007).

38 Weisse, J. M., Lee, C. H., Kim, D. R. & Zheng, X. Fabrication of Flexible and Vertical Silicon Nanowire Electronics. *Nano Lett.* **12**, 3339-3343 (2012).

39 Cui, Y., Zhong, Z., Wang, D., Wang, W. U. & Lieber, C. M. High Performance Silicon Nanowire Field Effect Transistors. *Nano Lett.* **3**, 149-152 (2003).

40 Custer, J. P. et al. Ratcheting quasi-ballistic electrons in silicon geometric diodes at room temperature. *Science.* **368**, 177 (2020).

41 Chou, L.-W., Boyuk, D. S. & Filler, M. A. Optically Abrupt Localized Surface Plasmon Resonances in Si Nanowires by Mitigation of Carrier Density Gradients. *ACS Nano* **9**, 1250-1256 (2015).

42 Kramer, N. J., Schramke, K. S. & Kortshagen, U. R. Plasmonic Properties of Silicon Nanocrystals Doped with Boron and Phosphorus. *Nano Lett.* **15**, 5597-5603 (2015).

43 Reece, S. Y. et al. Wireless solar water splitting using silicon-based semiconductors and earth-abundant catalysts. *Science.* **334**, 645-648 (2011).

44 Cuevas, A. The Recombination Parameter J_0. *Energy Procedia* **55**, 53-62 (2014).

45 Sze, S. M. & Ng, K. K. *Physics of Semiconductor Devices*. 3rd edn, (Wiley-Interscience, Hoboken, N.J., 2007).

46 Kempa, T. J. et al. Single and tandem axial p-i-n nanowire photovoltaic devices. *Nano Lett.* **8**, 3456-3460 (2008).

47 Hill, D. J., Teitsworth, T. S., Ritchie, E. T., Atkin, J. M. & Cahoon, J. F. Interplay of surface recombination and diode geometry for the performance of axial p–i–n nanowire solar cells. *ACS Nano* **12**, 10554-10563 (2018).

48 Mohite, A. D. et al. Highly efficient charge separation and collection across in situ doped axial VLS-grown Si nanowire p–n junctions. *Nano Lett.* **12**, 1965-1971 (2012).

49 Jung, Y., Vacic, A., Perea, D. E., Picraux, S. T. & Reed, M. A. Minority carrier lifetimes and surface effects in VLS-grown axial p–n junction silicon nanowires. *Adv. Mater.* **23**, 4306-4311 (2011).

50 Gabriel, M. M. et al. Imaging charge separation and carrier recombination in nanowire p-i-n junctions using ultrafast microscopy. *Nano Lett.* **14**, 3079-3087 (2014).

51 Christesen, J. D. et al. Design principles for photovoltaic devices based on Si nanowires with axial or radial p–n junctions. *Nano Lett.* **12**, 6024-6029 (2012).

52 Esaki, L. New Phenomenon in Narrow Germanium *p-n* Junctions. *Phys. Rev.* **109**, 603-604 (1958).

53 Kane, E. O. Theory of Tunneling. *J. Appl. Phys.* **32**, 83-91 (1961).

54 Sah, C. T. Electronic Processes and Excess Currents in Gold-Doped Narrow Silicon Junctions. *Phys. Rev.* **123**, 1594-1612 (1961).

55 Schenk, A. Rigorous theory and simplified model of the band-to-band tunneling in silicon. *Solid-State Electron.* **36**, 19-34 (1993).

56 Chynoweth, A. G., Logan, R. A. & Thomas, D. E. Phonon-Assisted Tunneling in Silicon and Germanium Esaki Junctions. *Phys. Rev.* **125**, 877-881 (1962).

57 Quaschning, V. & Hanitsch, R. Numerical simulation of current-voltage characteristics of photovoltaic systems with shaded solar cells. *Solar Energy* **56**, 513-520 (1996).

58 Hill, D. J., Teitsworth, T. S., Kim, S., Christesen, J. D. & Cahoon, J. F. Encoding highly nonequilibrium boron concentrations and abrupt morphology in p-type/n-type silicon nanowire superlattices. *ACS Appl. Mater. Interfaces* **9**, 37105-37111 (2017).

59 Vick, G. L. & Whittle, K. M. Solid Solubility and Diffusion Coefficients of Boron in Silicon. *J. Electrochem. Soc.* **116**, 1142 (1969).

60 Li, N., Tan, T. Y. & Gösele, U. Transition region width of nanowire hetero- and pn-junctions grown using vapor–liquid–solid processes. *Appl. Phys. A* **90**, 591-596 (2008).

61 Christesen, J. D., Pinion, C. W., Zhang, X., McBride, J. R. & Cahoon, J. F. Encoding abrupt and uniform dopant profiles in vapor–liquid–solid nanowires by suppressing the reservoir effect of the liquid catalyst. *ACS Nano* **8**, 11790-11798 (2014).

62 Ritchie, E. T. et al. Mapping free-carriers in multijunction silicon nanowires using infrared near-field optical microscopy. *Nano Lett.* **17**, 6591-6597 (2017).

63 Taubner, T., Hillenbrand, R. & Keilmann, F. Performance of visible and mid-infrared scattering-type near-field optical microscopes. *J. Microsc.* **210**, 311-314 (2003).

64 Gray, J. L. in *Handbook of Photovoltaic Science and Engineering* (eds A. Luque & S. Hegedus) Ch. 3, (2003).

65 Green, M. A. Self-consistent optical parameters of intrinsic silicon at 300K including temperature coefficients. *Solar Energy Materials and Solar Cells* **92**, 1305-1310 (2008).

66 Huang, Z., Geyer, N., Werner, P., de Boor, J. & Gösele, U. Metal-Assisted Chemical Etching of Silicon: A Review. *Adv. Mater.* **23**, 285-308 (2011).

67 Heitsch, A. T., Fanfair, D. D., Tuan, H.-Y. & Korgel, B. A. Solution−Liquid−Solid (SLS) Growth of Silicon Nanowires. *J. Am. Chem. Soc.* **130**, 5436-5437 (2008).

68 Schmidt, V., Wittemann, J. V., Senz, S. & Gösele, U. Silicon Nanowires: A Review on Aspects of their Growth and their Electrical Properties. *Adv. Mater.* **21**, 2681-2702 (2009).

69 Wagner, R. S. & Ellis, W. C. Vapor-liquid-solid Mechanism of Single Crystal Growth. *Appl. Phys. Lett.* **4**, 89-90 (1964).

70 Christensen, J. S., Radamson, H. H., Kuznetsov, A. Y. & Svensson, B. G. Phosphorus and boron diffusion in silicon under equilibrium conditions. *Appl. Phys. Lett.* **82**, 2254-2256 (2003).

71 Amit, I. et al. Spatially Resolved Correlation of Active and Total Doping Concentrations in VLS Grown Nanowires. *Nano Lett.* **13**, 2598-2604 (2013).

72 Schmid, H., Bessire, C., Björk, M. T., Schenk, A. & Riel, H. Silicon Nanowire Esaki Diodes. *Nano Lett.* **12**, 699-703 (2012).

73 Kim, S. et al. Designing morphology in epitaxial silicon nanowires: the role of gold, surface chemistry, and phosphorus doping. *ACS Nano* **11**, 4453-4462 (2017).

74 Cordoba, C., Teitsworth, T. S., Yang, M., Cahoon, J. F. & Kavanagh, K. Abrupt degenerately-doped silicon nanowire tunnel junctions. *Nanotechnol.* **31**, 415708 (2020).

75 Lichte, H. & Lehmann, M. Electron holography—basics and applications. *Rep. Prog. Phys.* **71**, 016102 (2007).

76 Darbandi, A., McNeil, J. C., Akhtari-Zavareh, A., Watkins, S. P. & Kavanagh, K. L. Direct Measurement of the Electrical Abruptness of a Nanowire p–n Junction. *Nano Lett.* **16**, 3982-3988 (2016).

77 Dupré, L., Buttard, D., Leclere, C., Renevier, H. & Gentile, P. Gold Contamination in VLS-Grown Si Nanowires: Multiwavelength Anomalous Diffraction Investigations. *Chem. Mater.* **24**, 4511-4516 (2012).

78 Meyer, E. L. Extraction of Saturation Current and Ideality Factor from Measuring V_{oc} and I_{sc} of Photovoltaic Modules. *Int. J. Photoenergy* **2017**, 8479487 (2017).

79 Koren, E. et al. Obtaining Uniform Dopant Distributions in VLS-Grown Si Nanowires. *Nano Lett.* **11**, 183-187 (2011).

80 Jiao, Y., Zheng, Y., Jaroniec, M. & Qiao, S. Z. Design of electrocatalysts for oxygen- and hydrogen-involving energy conversion reactions. *Chem. Soc. Rev.* **44**, 2060-2086 (2015).

81 Nørskov, J. K. et al. Trends in the Exchange Current for Hydrogen Evolution. *J. Electrochem. Soc.* **152**, J23 (2005).

82 Man, I. C. et al. Universality in Oxygen Evolution Electrocatalysis on Oxide Surfaces. *ChemCatChem* **3**, 1159-1165 (2011).

83 McCrory, C. C. L., Jung, S., Peters, J. C. & Jaramillo, T. F. Benchmarking Heterogeneous Electrocatalysts for the Oxygen Evolution Reaction. *J. Am. Chem. Soc.* **135**, 16977-16987 (2013).

84 Nørskov, J. K. et al. Origin of the Overpotential for Oxygen Reduction at a Fuel-Cell Cathode. *J. Phys. Chem. B.* **108**, 17886-17892 (2004).

85 Takata, T., Pan, C., Nakabayashi, M., Shibata, N. & Domen, K. Fabrication of a Core–Shell-Type Photocatalyst via Photodeposition of Group IV and V Transition Metal Oxyhydroxides: An Effective Surface Modification Method for Overall Water Splitting. *J. Am. Chem. Soc.* **137**, 9627-9634 (2015).

86 Wang, D. et al. Wafer-Level Photocatalytic Water Splitting on GaN Nanowire Arrays Grown by Molecular Beam Epitaxy. *Nano Lett.* **11**, 2353-2357 (2011).

87 Ran, J., Zhang, J., Yu, J., Jaroniec, M. & Qiao, S. Z. Earth-abundant cocatalysts for semiconductor-based photocatalytic water splitting. *Chem. Soc. Rev.* **43**, 7787-7812 (2014).

88 Simon, T., Carlson, M. T., Stolarczyk, J. K. & Feldmann, J. Electron Transfer Rate vs Recombination Losses in Photocatalytic H_2 Generation on Pt-Decorated CdS Nanorods. *ACS Energy Lett.* **1**, 1137-1142 (2016).

89 Wolff, C. M. et al. All-in-one visible-light-driven water splitting by combining nanoparticulate and molecular co-catalysts on CdS nanorods. *Nat. Energy* **3**, 862-869 (2018).

90 Li, R. et al. Spatial separation of photogenerated electrons and holes among {010} and {110} crystal facets of $BiVO_4$. *Nat. Commun.* **4**, 1432 (2013).

91 Wenderich, K. & Mul, G. Methods, Mechanism, and Applications of Photodeposition in Photocatalysis: A Review. *Chem. Rev.* **116**, 14587-14619 (2016).

92 Chen, R., Fan, F., Dittrich, T. & Li, C. Imaging photogenerated charge carriers on surfaces and interfaces of photocatalysts with surface photovoltage microscopy. *Chem. Soc. Rev.* **47**, 8238-8262 (2018).

93 Latorre-Sánchez, M., Primo, A., Atienzar, P., Forneli, A. & García, H. p–n Heterojunction of Doped Graphene Films Obtained by Pyrolysis of Biomass Precursors. *Small* **11**, 970-975 (2015).

94 Wang, J. et al. A silicon nanowire as a spectrally tunable light-driven nanomotor. *Adv. Mater.* **29**, 1701451 (2017).

95 Chen, Z., Dinh, H. N. & Miller, E. *Photoelectrochemical Water Splitting: Standards, Experimental Methods, and Protocols*. (Springer, New York, 2013).

96 Walter, M. G. et al. Solar Water Splitting Cells. *Chem. Rev.* **110**, 6446-6473 (2010).

97 Su, Y. et al. Single-nanowire photoelectrochemistry. *Nat. Nanotechnol.* **11**, 609-612 (2016).

98 Gerken, J. B. et al. Electrochemical water oxidation with cobalt-based electrocatalysts from pH 0–14: the thermodynamic basis for catalyst structure, stability, and activity. *J. Am. Chem. Soc.* **133**, 14431-14442 (2011).

99 Kempa, T. J. et al. Coaxial multishell nanowires with high-quality electronic interfaces and tunable optical cavities for ultrathin photovoltaics. *Proc. Natl. Acad. Sci.* **109**, 1407 (2012).

100 Krogstrup, P. et al. Single-nanowire solar cells beyond the Shockley–Queisser limit. *Nat. Photon.* **7**, 306-310 (2013).

101 Si, F. T., Isabella, O. & Zeman, M. Too Many Junctions? A Case Study of Multijunction Thin-Film Silicon Solar Cells. *Adv. Sustain. Syst.* **1**, 1700077 (2017).

102 Cao, L. et al. Engineering light absorption in semiconductor nanowire devices. *Nat. Mater.* **8**, 643-647 (2009).

103 Holmberg, V. C., Bogart, T. D., Chockla, A. M., Hessel, C. M. & Korgel, B. A. Optical properties of silicon and germanium nanowire fabric. *J. Phys. Chem. C* **116**, 22486-22491 (2012).

104 Kim, S. & Cahoon, J. F. Geometric nanophotonics: light management in single nanowires through morphology. *Acc. Chem. Res.* **52**, 3511-3520 (2019).

105 Kim, S., Kim, K.-H. & Cahoon, J. F. Optical Bound States in the Continuum with Nanowire Geometric Superlattices. *Phys. Rev. Lett.* **122**, 187402 (2019).

106 Zhang, H., Kumagai, A., Xu, G. & Ishibashi, K. Low-Temperature Atomic Hydrogen Treatment of SiO_2/Si Structures. *Jpn. J. Appl. Phys.* **42**, 6252-6255 (2003).

107 Kanan, M. W. & Nocera, D. G. In Situ Formation of an Oxygen-Evolving Catalyst in Neutral Water Containing Phosphate and Co^{2+}. *Science.* **321**, 1072 (2008).

108 Lutterman, D. A., Surendranath, Y. & Nocera, D. G. A Self-Healing Oxygen-Evolving Catalyst. *J. Am. Chem. Soc.* **131**, 3838-3839 (2009).

109 Wilson, B. C. & Adam, G. A Monte Carlo model for the absorption and flux distributions of light in tissue. *Med. Phys.* **10**, 824-830 (1983).

110 Flock, S. T., Patterson, M. S., Wilson, B. C. & Wyman, D. R. Monte Carlo modeling of light propagation in highly scattering tissues. I. Model predictions and comparison with diffusion theory. *IEEE. Trans. Biomed. Eng.* **36**, 1162-1168 (1989).

111 Wu, Y., Lin, X., Wu, Z., Möhwald, H. & He, Q. Self-Propelled Polymer Multilayer Janus Capsules for Effective Drug Delivery and Light-Triggered Release. *ACS Appl. Mater. Interfaces* **6**, 10476-10481 (2014).